

AD \_\_\_\_\_

Award Number: DAMD17-00-1-0291

TITLE: A Training Program in Breast Cancer Research Using NMR  
Techniques

PRINCIPAL INVESTIGATOR: Paul C. Wang, Ph.D.

CONTRACTING ORGANIZATION: Howard University  
Washington, DC 20059

REPORT DATE: July 2004

TYPE OF REPORT: Annual

PREPARED FOR: U.S. Army Medical Research and Materiel Command  
Fort Detrick, Maryland 21702-5012

DISTRIBUTION STATEMENT: Approved for Public Release;  
Distribution Unlimited

The views, opinions and/or findings contained in this report are those of the author(s) and should not be construed as an official Department of the Army position, policy or decision unless so designated by other documentation.

20050105 020

# REPORT DOCUMENTATION PAGE

Form Approved  
OMB No. 074-0188

Public reporting burden for this collection of information is estimated to average 1 hour per response, including the time for reviewing instructions, searching existing data sources, gathering and maintaining the data needed, and completing and reviewing this collection of information. Send comments regarding this burden estimate or any other aspect of this collection of information, including suggestions for reducing this burden to Washington Headquarters Services, Directorate for Information Operations and Reports, 1215 Jefferson Davis Highway, Suite 1204, Arlington, VA 22202-4302, and to the Office of Management and Budget, Paperwork Reduction Project (0704-0188), Washington, DC 20503

<b>1. AGENCY USE ONLY</b> (Leave blank)	<b>2. REPORT DATE</b> July 2004	<b>3. REPORT TYPE AND DATES COVERED</b> Annual (1 Jul 03 - 30 Jun 04)	
<b>4. TITLE AND SUBTITLE</b> A Training Program in Breast Cancer Research Using NMR Techniques		<b>5. FUNDING NUMBERS</b> DAMD17-00-1-0291	
<b>6. AUTHOR(S)</b> Paul C. Wang, Ph.D.		<b>8. PERFORMING ORGANIZATION REPORT NUMBER</b>	
<b>7. PERFORMING ORGANIZATION NAME(S) AND ADDRESS(ES)</b> Howard University Washington, DC 20059  E-Mail: pwang@howard.edu			
<b>9. SPONSORING / MONITORING AGENCY NAME(S) AND ADDRESS(ES)</b> U.S. Army Medical Research and Materiel Command Fort Detrick, Maryland 21702-5012		<b>10. SPONSORING / MONITORING AGENCY REPORT NUMBER</b>	
<b>11. SUPPLEMENTARY NOTES</b>			
<b>12a. DISTRIBUTION / AVAILABILITY STATEMENT</b> Approved for Public Release; Distribution Unlimited			<b>12b. DISTRIBUTION CODE</b>
<b>13. ABSTRACT (Maximum 200 Words)</b>  This program has supported four predoctoral students (two students from the Electrical Engineering Department, one medical student and one MD/PhD student from Biochemistry) and three postdoctoral fellows. The new students have been introduced to the Biomedical NMR Laboratory and the Howard University Cancer Center. The trainees have continued to learn the theories and instrumentation behind nuclear MRI. The trainees have rotated through the mammography service in the Radiology Department to learn mammography procedures. Besides attending weekly seminars in the Cancer Center, the trainees also have attended a special seminar series on breast imaging sponsored by this grant. Each trainee has actively participated in research projects. Based on the experimental findings, two papers were published and another one has been accepted for publication. Three abstracts have been presented and another two will be presented later this year in the national and international scientific meetings. Two predoctoral students received BS degrees and will attend graduate schools to continue biomedical imaging research. Two new research initiatives have been developed to do molecular imaging of breast cancer and to establish a breast cancer image database for computer-aided-diagnosis research. We have submitted four grant applications—two have received funding and the other two are pending.			
<b>14. SUBJECT TERMS</b> Training, Nuclear Magnetic Resonance, Breast Cancer			<b>15. NUMBER OF PAGES</b> 53
<b>17. SECURITY CLASSIFICATION OF REPORT</b> Unclassified			<b>16. PRICE CODE</b>
			<b>20. LIMITATION OF ABSTRACT</b>  Unlimited
<b>18. SECURITY CLASSIFICATION OF THIS PAGE</b> Unclassified	<b>19. SECURITY CLASSIFICATION OF ABSTRACT</b> Unclassified		

NSN 7540-01-280-5500

Standard Form 298 (Rev. 2-89)  
Prescribed by ANSI Std. Z39-18  
298-102

## Table of Contents

<b>Cover.....</b>	<b>1</b>
<b>SF 298.....</b>	<b>2</b>
<b>Table of Contents.....</b>	<b>3</b>
<b>Introduction.....</b>	<b>4</b>
<b>Body.....</b>	<b>4</b>
<b>Key Research Accomplishments.....</b>	<b>6</b>
<b>Reportable Outcomes.....</b>	<b>7</b>
<b>Conclusions.....</b>	<b>9</b>
<b>References.....</b>	<b>10</b>
<b>Appendices.....</b>	<b>11</b>

## **I. Introduction**

This is the fourth year of the training grant, which supports predoctoral students and postdocs for pursuing breast cancer research using NMR techniques. There are four predoctoral students (Shani Ross, O'tega Ejofodomi, Emmanuel Agwu, and Raymond Malveaux) and three postdoctoral research associates (Ercheng Li, Renshu Zhang and Lisa Kinnard) supported by this grant. Shani Ross and O'tega Ejofodomi are seniors in the Department of Electrical Engineering. Dr. Emmanuel Agwu is a 4<sup>th</sup> PhD student (the 8<sup>th</sup> year in the MD/PhD program) from the Department of Molecular Biology and Biochemistry. Dr. Agwu has finished his M.D. program and is continuing his Ph.D. program. Raymond Malveaux is a third year medical student who started research in this lab during the summer of 2003. Dr. Lisa Kinnard graduated from the Department of Electrical Engineering in June 2003 and continued as a postdoctoral fellow at Howard University Cancer Center. Dr. Ercheng Li is a NMR/MRI specialist. Dr. Renshu Zhang is a radiologist. Both Dr. Li and Dr. Zhang are research associates.

All the trainees have rotated through the mammography service in the Department of Radiology to learn the mammography procedures. Besides attending the weekly seminars in the Cancer Center, the trainees also have attended a special seminar series on breast imaging sponsored by this grant and the Department of Electrical Engineering. Dr. Li and Dr. Zhang have also attended the annual meeting of the AACR (Association of American Cancer Research). Each trainee has actively participated in one of the research projects. Based on the experimental findings, three papers were published. Three abstracts have been presented and two other abstracts will be presented to national and international scientific meetings. A list of the publications and presentations are included in the reportable outcomes section. The PI has submitted three grant applications. One has been funded and the other two are in pending. Dr. Kinnard has also received a postdoctoral grant from the USAMRMC.

## **II. Body**

In the 4<sup>th</sup> year, we conducted studies in two key research areas: (1) imaging processing techniques to separate the malignant and benign masses on digital mammograms (2) the role of P-glycoprotein modulation in drug-drug interaction. We have also started two new research projects: (3) Establishment of an Image Database for Computer-Aided-Diagnosis (CAD) research development (Dr. Lisa Kinnard, Shani Ross and O'tega Ejofodomi ) (4) Tumor-targeted MR contrast enhancement by anti-transferrin receptor scFv-Immunoliposome nanoparticles. (Dr. Ercheng Li and Dr. Zhang)

### **Continued Research Projects:**

- (1) Segmentation of Mammographic Masses Project (Dr. Kinnard)

Mammography combined with clinical examination is a standard method used for the detection and diagnosis of breast cancer. However, mammography alone can produce a high percentage of false positives. A computer-aided diagnostic (CAD<sub>x</sub>) system can serve as a more accurate clinical tool for the radiologist, consequently lowering the rate of missed breast cancer and ultimately lowering morbidity and mortality. Breast cancer can exist not only in the form of

masses, but also in the forms of microcalcifications, asymmetric density, and architectural distortion. These abnormalities can be seen using imaging techniques such as mammography, ultrasound and magnetic resonance imaging (MRI). Breast images have different appearances based upon their amounts of fibroglandular and fatty tissue. Masses can have unclear borders and sometimes overlap with glandular tissue in mammograms, therefore the radiologists may overlook these masses during their search of suspicious areas. Proper segmentation to include the shape and boundary characteristics is an essential step in aiding the computer for the analysis and malignancy determination of the mass. While many CAD<sub>x</sub> systems have been developed, the development of effective image segmentation algorithms for breast masses remains unsolved in this field, particularly in the cases where the breast tissue is dense. Since cancerous masses often appear to be light and have ill-defined borders, it is quite challenging for mammographers to extract them from surrounding tissue. It is even more difficult to automatically segment masses from dense tissue. In this research, a fully automated segmentation algorithm has been developed. It delineates the complete masses with minimum normal structures in dense and mixed tissue mammograms.

(2) P-glycoprotein Modulation Project (Dr. Agwu, Dr. Li, Dr. Zhang, Malveaux)

Cancer patients are often treated with combination therapy for secondary symptoms such as depression, and cardiopulmonary diseases. The potential for drug-drug interaction under these conditions is high. Such interactions may cause changes in the pharmacokinetics, especially for drugs with narrow therapeutic indices. These changes can alter efficacy and toxicity of the administered drugs. Drug-drug interactions may occur due to common metabolic pathways, but are also a result of interference at the P-glycoprotein (Pgp) level. Pgp, which is a nonspecific transport protein, is expressed constitutively at the blood-brain-barrier (BBB), intestine, kidney, liver, and in activated T-cells. Interaction at the blood-brain-barrier may occur if one of the two concomitantly administered drugs blocks Pgp, thus allowing the other drug to penetrate the brain freely. The potential for drug-drug interactions is not routinely studied at the Pgp level during drug development. Its presence is assumed only after unexpected clinical symptoms arise. In this study, we have demonstrated the drug penetration through the blood-brain-barrier due to Pgp modulation using a dynamic NMR method based on detection of a fluorinated drug, trifluoperazine (TFP).

**New Research Projects:**

(3) Establishment of an Image Database for Computer-Aided-Diagnosis (CAD) Research Development. (Dr. Lisa Kinnard, Shani Ross and O'tega Ejofodomi)

The success of CAD is based on the accuracy and completeness of the mammographic image database, of which the CAD extracts the features of different types of pathology. The current available mammographic image databases are all obtained from the Caucasian population. There are very few African American cases. It is well known that African American women generally have denser breasts. The appearance of mammograms from African American breast cancer patients may not be the same as those images from Caucasian breast cancer patients. Howard University Cancer Center has a well maintained cancer registry. It has more than 200 new African American breast cancer cases each year. We have digitized 1000 mammograms from 220 patients' records. Our intention is to

establish a breast cancer image database based on this African American population. This database will be available on the internet to the CAD software developers and researchers.

(4) Tumor-targeted MR Contrast Enhancement by Anti-transferrin Receptor scFv-Immunoliposome Nanoparticles. (Dr. Li, Dr. Zhang)

In recent years, advances in molecular and cell biology techniques have had a marked effect on our understanding of the cellular and molecular mechanisms of cancers including breast cancer. Significant efforts have also been made toward the development of a noninvasive, high-resolution in vivo imaging technology such as positron emission tomography (PET), magnetic resonance imaging (MRI), and optical imaging techniques for the better imaging of tumors. In vivo molecular imaging, which utilizes these two fronts, opens up an extraordinary opportunity for studying diseases noninvasively and—in many cases—quantitatively at the molecular level. The success of molecular imaging will lead to an understanding of the molecular changes that underlie the diseases, and, may potentially lead to the early detection of breast cancer.

Magnetic resonance molecular imaging strategies have been explored by specifically targeting oncogenes such as HER-2 (c-erbB-2, Neu), bcl-2/bcl-xL, protein kinase A, and the transferrin receptor gene. The human transferrin receptor (hTfR) has been used as a molecular target to direct therapeutic agents to tumor cells and to shuttle drugs across the blood-brain barrier. NMR imaging can visualize expression and regulation of hTfR receptors by studying the receptors with a sterically protecting iron-containing magnetic hTfR probe. A cationic immunoliposome system, which covalently conjugates the single-chain antibody variable region fragment (scFv) against the hTfR has been used to improve p53 tumor suppressor gene therapy employed in the human breast cancer metastasis model. This scFv-immunoliposome can systematically deliver the complexed gene to tumors in vivo. In comparison to a whole antibody or transferrin molecule, scFv has a much smaller size, enabling it to penetrate more easily through solid tumors. In this study we will utilize the TfR scFv-immunoliposome along with MR contrast agents to improve contrast agent-tumor affinity and specificity. This will enhance MR diagnostic imaging capabilities, particularly those needed for early detection.

### III. Key Research Accomplishments

#### Statement of Work: (expected in year 4)

##### Predoctoral Student:

- **Conclude the thesis project and write up thesis**

Ms. Shani Ross and Ms. O'tega Ejofodomi finished their senior research projects and graduated in June 2004. Dr. Emmanuel Agwu finished medical school and he is in the 4th year of his PhD program. Dr. Agwu is continuing pursuing his doctoral thesis research. Dr. Agwu's research has been delayed due to his health condition. Dr. Agwu is originally from Nigeria. He has an inherited sickle cell disease. After his graduation from the medical school last summer, he has experienced four severe crises and had to be hospitalized for few days to a few weeks throughout the year. He has participated in a NIH clinical trial for sickle cell disease. The PI and his thesis committee members have discussed the situation and decided

not to put any extra pressure on him under this special circumstance. The thesis committee agrees that he has been a responsible and intelligent student throughout the past few years in his MD/PhD program. The thesis committee would like to support him to continue his PhD program. Dr. Agwu plans to finish his research work by the end of 2004 and write up the thesis in the spring of 2005. The PI has submitted an extension of this grant, which is supposed to end by June 30, 2004 in order to continue to support this student and the research.

- **Thesis defense and writing of scientific papers for publication**

Dr. Agwu's research has slowed down because of his health condition. He will finish his thesis in the spring of 2005 and graduate in June 2005. He plans to publish his PhD work and present the research results at the AACR meeting.

Postdoctoral Student:

- **Select a new research project approved by the Executive Committee**

There are two new research projects that have been developed and approved by the Executive Committee:

- (1) Establishment of an Image Database for Computer-Aided-Diagnosis (CAD) Research Development. (Dr. Lisa Kinnard)
- (2) Tumor-targeted MR Contrast Enhancement by Anti-transferrin Receptor scFv-Immunoliposome Nanoparticles. (Dr. Ercheng Li and Dr. Zhang)

- **Clinical preceptorship (half a day per week)**

Dr. Li and Dr. Zhang have worked with radiologists in the Department of Radiology to study breast cancer image patterns, clinically indeterminate cases, image pattern analysis of masses vs. microcalcifications, and biopsy procedures.

- **Conduct the new research project**

- (1) We have been digitized 1,000 mammograms from 220 breast cancer patients as an important initial step for establishing a web-based breast cancer image database. The intended database will be available on the internet and will be used for CAD software development and teaching purposes.
- (2) Dr. Li and Dr. Zhang have conducted a proof-of-principle study to validate the proposed MRI image contrast enhancement strategy using immunoliposomes attached with specialized ligands to recognize transferrin receptors, which are overly expressed on breast cancer cells.

- **Present progress report to the Executive Committee once every six months**

The progress of the research was reported to the Executive Committee routinely.

- **Present research results to the Cancer Center faculty and National Meeting**

Three papers have been presented in the national and international meetings. Two other papers have been accepted for presentation later this year.

- **Writing Scientific papers**

The trainees and PI have published two papers and the third paper has been accepted for publication. The titles of the scientific papers are listed in the reportable outcomes.

#### IV. REPORTABLE OUTCOMES

**Papers:**

1. Kinnard L, Lo SB, Makariou E, Osicka T, Wang PC, Freeman M, Chouikha M. Likelihood Function Analysis For Segmentation of Mammographic Masses For Various Margin Groups. Proc of IEEE Symposium on Biomedical Imaging. pp 113-116, 2004.
2. Liang XJ, Yin JJ, Zhou JW, Wang PC, Taylor B, Cardarelli C, Kozar M, Forte R, Aszalos A, Gottesman M. Lipid Composition and Biophysical Differences in the Plasma Membrane Relate to Cisplatin Resistance in Human Epidermal Carcinoma Cells. Exp Cell Research 293:283-291, 2004.
3. Kinnard L, Lo SB, Makariou E, Osicka T, Wang PC, Chouikha M, Freeman M. Steepest Changes of a Probability-based Cost Function for Delineation of Mammographic Masses: A Validation Study. Med Phys 2004 (accepted for publication)

#### **Presentations:**

1. Wang PC, Aszalos A, Li E, Zhang R, Song H. A Pharmacokinetic Study of Trifluoperazine Crossing Blood-Brain-Barrier Due to P-glycoprotein Modulation. ISMRM, Workshop on Dynamic Spectroscopy and Measurement of Physiology and Function. September 6-8, 2003, Orlando, FL.
2. Kinnard L, Lo SB, Makariou E, Osicka T, Wang PC, Freeman M, Chouikha M. Likelihood Function Analysis For Segmentation of Mammographic Masses For Various Margin Groups. International Society of Biomedical Imaging, April 15-18, 2004, Arlington, VA.
3. Wang PC, Aszalos A, Li E, Zhang R, Song H, Malveaux R. A NMR Study of Trifluoperazine Crossing Blood-Brain-Barrier Due to P-glycoprotein Modulation. ISMRM 12<sup>th</sup> Annual Meeting, May 17-21, 2004, Kyoto, Japan.
4. Wang PC, Li E, Zhang R, Song H, Pirolo K, Chang EH. MR Image Enhancement by Tumor Cell Targeted Immunoliposome Complex Delivered Contrast Agent. Society for Molecular Imaging 3<sup>rd</sup> Annual Meeting, September 9-12, 2004, St. Louis, MO.
5. Manaye KF, Wang PC, O'Neil J, Oei A, Song H, Tizabi Y, Ingram DK, Mouton PR. In vivo and In vitro Stereological Analysis of Hippocampal and Brain Volumes in Young and Old APP/PS1 Mice Using Magnetic Resonance Neuroimages. Society of Neuroscience 34<sup>th</sup> Annual Meeting, October 23-27, 2004 San Diego, CA.

#### **Degrees Awarded:**

1. Ms. Shani Ross received her B.S. degree in June 2004 from the Department of Electrical Engineering. She is going to the graduate program in the Department of Biomedical Engineering at the University of Michigan.
2. Ms. O'tega Ejofodomi received her B.S. degree in June 2004 from the Department of Electrical Engineering. She is going to the graduate program in the Department of Electrical Engineering at the Howard University pursuing medical imaging research.

#### **Funding Applied and Received:**

Received:

1. 06/04-05/05 Tumor-targeted MR Contrast Enhancement by Anti-transferrin Receptor scFV-Immunoliposome Nanoparticles. Dr. Paul Wang is the principal investigator of this pilot project, which is funded through a Johns Hopkins center grant (NIH SPORE, P50 CA88843-04). Dr. Nancy Davidson is the PI of the program.
2. 07/03-06/05 Automatic Segmentation of Malignant and Benign Masses in Dense Breast Tissue, Dr. Lisa Kinnard is the PI of this postdoctoral grant, which is funded by USAMRMC (DAMD17-03-1-0314).

**Applied:**

1. A Partnership Training Program in Breast Cancer Research Using Molecular Imaging Techniques (BC043167). This is a four year training grant partnership with the Johns Hopkins University, In vivo Cellulose and Molecular Imaging Center. The proposal was submitted to the U.S. Army Medical Research and Materiel Command
2. Tumor-targeted MR Contrast Enhancement Using Molecular Imaging Techniques. National Cancer Institute's Minority Institution/Cancer Center Partnership (MI/CCP) program Pilot Project Initiative (submitted on 03/22/04)

## **V. Conclusion**

In the fourth year, this program has supported four predoctoral students (two new students from the Electrical Engineering Department, one medical student and one MD/PhD student from Biochemistry) and three postdoctoral fellows. The MD/PhD student has suffered illness due to the inherited Sickle Cell disease. His PhD thesis work has been delayed. The graduate committee has discussed his special condition and granted him an extension for him to continue his pursuit. The PI has filed an extension of this grant (which will expire by June 30, 2004) in order to continue supporting the students and the research study. The new students have been introduced to the Biomedical NMR Laboratory and the Howard University Cancer Center. The trainees have continued to learn the theory and instrumentation of nuclear MRI. The trainees have rotated through the mammography service in the Radiology Department to learn mammography procedures. Besides attending weekly seminars in the Cancer Center, the trainees have also attended a special seminar series on breast imaging sponsored by this grant.

Each trainee has actively participated in one of the four research projects. Dr. Kinnard has developed a fully automated segmentation algorithm to delineate the complete masses with minimum normal structures in dense and mixed tissue mammograms. Drs. Li, Malveaux, and Zhang have demonstrated the drug penetration through the blood-brain-barrier due to P-glycoprotein modulation using a dynamic NMR method of detecting trifluoperazine in the brain. Shani Ross and O'tega Ejofodomi with Dr. Kinnard have digitized 1000 mammograms from 220 patients' records to establish an image database for CAD research and software development. Drs. Li and Zhang have developed a new MRI contrast enhancement method using molecular imaging technique specifically targeted to the cancer cells.

This year two papers were published and another one has been accepted for publication. Three abstracts have been presented and another two will be presented later this year to the national and international scientific meetings. Two predoctoral students who have received B.S. degrees will attend graduate schools to continue their biomedical imaging research. Two new research initiatives have been developed to conduct molecular imaging of breast cancer and to establish a breast cancer image database for computer-aided-diagnosis research. Four grant applications have been submitted. Two have received funding and the other two are pending.

## VI. References

1. Brake GM, Karssemeijer N, Segmentation of suspicious densities in digital mammograms, *Medical Physics*, 2001, vol. 28, no. 2, pp. 259-266.
2. Heath M, Bowyer KW, Kopans D et al, Current status of the Digital Database for Screening Mammography, *Digital Mammography*, Kluwer Academic Publishers, 1998, pp. 457-460.
3. Li H, Wang Y, Liu KJR, Lo S-C, Freedman MT, Computerized Radiographic Mass Detection - Part I: Lesion Site Selection by Morphological Enhancement and Contextual Segmentation, *IEEE Transactions on Medical Imaging*, 2001, vol. 20, no. 4, pp. 289-301.
4. Mendez AJ, Tahoces PG, Lado MJ, Souto M., Vidal JJ, Computer-aided diagnosis: Automatic detection of malignant masses in digitized mammograms, *Medical Physics*, 1998, vol. 25, no. 6, pp. 957-964.
5. Sahiner B, Chan HP, Wei D, Petrick N, Helvie MA, Adler DD, Goodsit MM, Image feature selection by a genetic algorithm: Application to classification of mass and normal breast tissue, *Medical Physics*, 1996, vol.23, no.10, pp.1671-1684.
6. Balis FM, Drug interaction of commonly used anticancer drugs. *Clin. Pharmacokin.*, 11, 223-235, 1986
7. Ibrahim S, Peggins J, Knapton A, Licht T, Aszalos A, Influence of beta-drenergic antagonists, H1-receptor blockers, analgesics, and quinolon antibiotics on the cellular accumulation of anticancer drug, daunorubicin: P-glycoprotein modulation. *Anticancer Res.*, 21, 847-856, 2001
8. Gottesman MM, Fojo T and Bates SE, Multidrug resistance in cancer: role of ATP-dependent transporters. *Nature Reviews*, 2, 48-58, 2002
9. Schinkel A, Wagenar F, Mol C and Van Deemter L, P-glycoprotein in the blood-brain-barrier of mice influences the brain penetration and pharmacological activity of many drugs. *J. Clin. Invest.*, 97,2517-2524, 1996
10. Tatsura T, Naito M, Ohhara T, Sugawara I and Tsuruo T, Functional involvment of P-glycoprotein in blood-brain-barrier. *J. Biol. Chem.*, 267,20383-20391, 1992
11. Weissleder R, Mahmood U. *Molecular Imaging. Radiology* 219:316-333, 2001.
12. Sharma V, Luker GD, Piwnica-Worms D. Molecular imaging of gene expression and protein function *in vivo* with PET and SPECT. *J Magn Reson Imag* 16:336-351, 2002
13. Louise AY, Huber MM, Ahrens ET, Rothbacher U, Moats R, Jacobs RE, Fraser SE, Meade TJ. *In vivo* visualization of gene expression using magnetic resonance imaging. *Nature Biotechnology* 18:321-325, 2000.
14. Moore A, Basilion JP, Ciocca A, Weissleder R. Measuring transferrin receptor gene expression by NMR imaging. *Biochemica Biophysica Acta* 1402:239-249, 1998.
15. Artemov D, Mori N, Ravi R, Bhujwala ZM, Magnetic resonance molecular imaging of the HER-2/neu receptor, *Cancer Research* 63: 2723-2727, 2003.
16. Xu L, Tang WH, Huang CC, Alexander W, Xiang LM, Pirollo KF, Rait A, Chang EH. Systemic p53 gene therapy of cancer with immunolipoplexes targeted by anti-transferrin receptor scFv. *Mol. Med.* 7:726-738, 2001.
17. Liang Xu, Cheng-Cheng Huang, Weiqun Huang, Wen-Hua Tang, Antonia Rait, Yu Zhi Yin, Idalia Criz, Lai-Man Xiang, Kathleen F. Pirollo, Ester H. Chang, Systemic tumor-targeted gene delivery by anti-transferrin receptor scFv-immunoliposomes. *Molecular Cancer Therapy*, 1:337-346, 2002.

## VII. Appendices

(Three published papers and four abstracts)

### Papers:

1. Kinnard L, Lo SB, Makariou E, Osicka T, Wang PC, Freeman M, Chouikha M. Likelihood Function Analysis For Segmentation of Mammographic Masses For Various Margin Groups. Proc of IEEE Symposium on Biomedical Imaging. pp 113-116, 2004.
2. Liang XJ, Yin JJ, Zhou JW, Wang PC, Taylor B, Cardarelli C, Kozar M, Forte R, Aszalos A, Gottesman M. Changes in Biophysical Parameters of Plasma Membranes Influence Cisplatin Resistance of Sensitive and Resistant Epidermal Carcinoma Cells. Exp Cell Research 293:283-291, 2004.
3. Kinnard L, Lo SB, Makariou E, Osicka T, Wang PC, Chouikha M, Freeman M. Steepest Changes of a Probability-based Cost Function for Delineation of Mammographic Masses: A Validation Study. Med Phys 2004 (accepted for publication)

### Presentations/Abstracts:

1. Wang PC, Aszalos A, Li E, Zhang R, Song H. A Pharmacokinetic Study of Trifluoperazine Crossing Blood-Brain-Barrier Due to P-glycoprotein Modulation. ISMRM, Workshop on Dynamic Spectroscopy and Measurement of Physiology and Function. September 6-8, 2003, Orlando, FL.
2. Wang PC, Aszalos A, Li E, Zhang R, Song H, Malveaux R. A NMR Study of Trifluoperazine Crossing Blood-Brain-Barrier Due to P-glycoprotein Modulation. ISMRM 12<sup>th</sup> Annual Meeting, May 17-21, 2004, Kyoto, Japan.
3. Wang PC, Li E, Zhang R, Song H, Pirollo K, Chang EH. MR Image Enhancement by Tumor Cell Targeted Immunoliposome Complex Delivered Contrast Agent. Society for Molecular Imaging 3<sup>rd</sup> Annual Meeting, September 9-12, 2004, St. Louis, MO.
4. Manaye KF, Wang PC, O'Neil J, Oei A, Song H, Tizabi Y, Ingram DK, Mouton PR. In vivo and In vitro Stereological Analysis of Hippocampal and Brain Volumes in Young and Old APP/PS1 Mice Using Magnetic Resonance Neuroimages. Society of Neuroscience 34<sup>th</sup> Annual Meeting, October 23-27, 2004 San Diego, CA.

## LIKELIHOOD FUNCTION ANALYSIS FOR SEGMENTATION OF MAMMOGRAPHIC MASSES FOR VARIOUS MARGIN GROUPS

*Lisa Kinnard<sup>a,b,c</sup>, Shih-Chung B. Lo<sup>a</sup>, Erini Makariou<sup>a</sup>, Teresa Osicka<sup>a,d</sup>, Paul Wang<sup>c</sup>,  
Matthew T. Freedman<sup>a</sup>, Mohamed Chouikha<sup>b</sup>*

<sup>a</sup>ISIS Center, Dept. of Radiology, Georgetown University Medical Center, Washington, D.C., USA

<sup>b</sup>Department of Electrical and Computer Engineering, Howard University, Washington, D.C., USA

<sup>c</sup>Biomedical NMR Laboratory, Department of Radiology, Howard University, Washington, D.C.,  
USA

<sup>d</sup>Department of Electrical Engineering and Computer Science, The Catholic University of America,  
Washington DC, USA

### ABSTRACT

The purpose of this work was to develop an automatic boundary detection method for mammographic masses and to observe the method's performance on different four of the five margin groups as defined by the ACR, namely, spiculated, ill-defined, circumscribed, and obscured. The segmentation method utilized a maximum likelihood steep change analysis technique that is capable of delineating ill-defined borders of the masses. Previous investigators have shown that the maximum likelihood function can be utilized to determine the border of the mass body. The method was tested on 122 digitized mammograms selected from the University of South Florida's Digital Database for Screening Mammography (DDSM). The segmentation results were validated using overlap and accuracy statistics, where the gold standards were manual traces provided by two expert radiologists. We have concluded that the intensity threshold that produces the best contour corresponds to a particular steep change location within the likelihood function.

### 1. INTRODUCTION

In a CAD<sub>x</sub> system, segmentation is arguably one of the most important aspects – particularly for masses – because strong diagnostic predictors for masses are shape and margin type [2,9]. The margin of a mass is defined as the interface between the mass and surrounding tissue [2]. Furthermore, breast masses can have unclear borders and are sometimes obscured by glandular tissue in mammograms. A spiculated mass consists of a central mass body surrounded by fibrous projections, hence the resulting stellate shape. For the aforementioned reasons, proper segmentation - to include the body and periphery - is extremely important and is essential for the computer to analyze, and in turn, determine the malignancy of the mass in mammographic CAD<sub>x</sub> systems.

Over the years researchers have used many methods to segment masses in mammograms. Petrick [7] et al. developed the Density Weighted Contrast Enhancement (DWCE) method, in which series of filters are applied to the image in an attempt to extract masses. Comer et al. [1] segmented digitized mammograms into

homogeneous texture regions by assigning each pixel to one of a set of classes such that the number incorrectly classified pixels was minimized via Maximum Likelihood (ML) analysis. Li [5] developed a method that employs k-means classification to classify pixels as belonging to the region of interest (ROI) or background.

Kupinski and Giger developed a method [4], which uses ML analysis to determine final segmentation. In their method, the likelihood function is formed from likelihood values determined by a set of image contours produced by the region growing method. This method is a highly effective one that was also implemented by Te Brake and Karssemeijer in their comparison between the discrete dynamic contour model and the likelihood method [9]. For this reason we chose to investigate its use as a possible starting point from which a second method could be developed. Consequently in our implementation of this work we discovered an important result, i.e., the maximum likelihood steep change. It appears that in many cases this method produces contour choices that encapsulate important borders such as mass spiculations and ill-defined borders.

### 2. METHODS

#### 2.1 Initial Contours

As an initial segmentation step, we followed the overall region similarity concept to aggregate the area of interest [1, 4]. Used alone, a sequence of contours representing the mass is generated; however, the computer is not able to choose the contour that is most closely correlated with the experts' delineations. Furthermore, we have devised an ML function steep change analysis method that chooses the best contour that delineates the mass body as well as its extended borders, i.e., extensions into spiculations and areas in which the borders are ill-defined or obscured. This method is an extension of the method developed by Kupinski and Giger [4] that uses ML function analysis to select the contour which best represents the mass, as compared to expert radiologist traces. We have determined that this technique can select the contour that accurately represents the mass body contour for a given set of parameters; however, further analysis of the likelihood function revealed that the computer could

choose a set of three segmentation contour choices from the entire set of contour choices, and then make a final decision from these three choices.

The algorithm can be summarized in several steps. Initially, we use an intensity based thresholding scheme to generate a sequence of grown contours ( $S_i$ ), where gray value is the similarity criterion. The image is also multiplied by a 2D trapezoidal membership function (2D shadow), whose upper base measures 40 pixels and lower base measures 250 pixels (1 pixel = 50 microns). The image to which the shadow has been applied is henceforth referred to as the "fuzzy" image. The original image and its fuzzy version were used to compute the likelihood of the mass's boundaries. The computation method is comprised of two components for a given boundary: (1) formulation of the composite probability and (2) evaluation of likelihood.

In addition, we chose to aggregate contours using the original image. This accounts for the major difference from that implemented by the previous investigators. Since smoother contours were not used, the likelihood function showed greater variations. In many situations, the greatest variations occurred when there was a sudden increase of the likelihood, and this was strongly correlated with the end of the mass border growth. This phenomenon would be suppressed if the fuzzy image was used to generate the contours. The fuzzy image was used mainly to construct the likelihood function.

## 2.2 Composite Probability Formation

For a contour ( $S_i$ ), the composite probability ( $C_i$ ) is calculated:

$$C_i|S_i = p(f_i(x, y)|S_i) \times p(m_i(x, y)|S_i) \quad (1)$$

The quantity  $f_i(x, y)$  is the area to which the 2D shadow has been multiplied,  $p(f_i(x, y)|S_i)$  is the probability density function of the pixels inside  $S_i$  where 'i' is the region growing step associated with a given intensity threshold. The quantity  $m_i(x, y)$  is the area outside  $S_i$  (non-fuzzy), and  $p(m_i(x, y)|S_i)$  is the probability density function of the pixels outside  $S_i$ . Next we find the logarithm of the composite probability of the two regions,  $C_i$ :

$$\text{Log}(C_i|S_i) = \log(p(f_i(x, y)|S_i)) + \log(p(m_i(x, y)|S_i)) \quad (2)$$

## 2.3 Evaluation of Likelihood Function

The likelihood that the contour represents the fibrous portion of the mass, i.e., mass body is determined by assessing the maximum likelihood function:

$$\arg \max (\text{Log}(C_i|S_i)), S_i, i = 1, \dots, n \quad (3)$$

Equation (3) intends to find the maximum value of the aforementioned likelihood values as a function of intensity threshold. It has been assessed (also by other investigators [4]) that the intensity value corresponding to this maximum likelihood value is the optimal intensity needed to delineate the mass body contour. However, in our implementation it was discovered that the intensity threshold corresponding to the maximum likelihood value confines the contour to the mass body. In our study many of these contours did not include the extended borders. We, therefore, hypothesize that the contour represents the mass's extended borders may well be determined by assessing the maximum changes of the likelihood function, i.e., locate the steepest likelihood value changes within the function:

$$\frac{d}{di} (\text{Log}(C_i|S_i)), S_i, i = 1, \dots, n \quad (4)$$

Based on this assumption, we have carefully analyzed the behavior of maximum likelihood function. The analysis reveals that we have successfully discovered that the most accurate mass delineation is usually obtained by using the intensity value corresponding to the first or second steep change locations within the likelihood function immediately following the maximum likelihood value on the likelihood function.

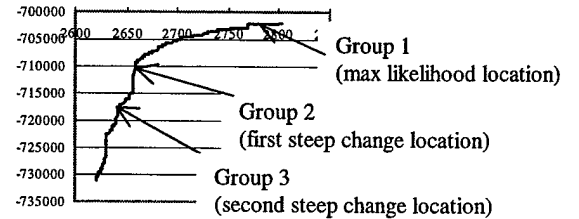


Figure 1: A likelihood function with steep change indicators

## 2.4 Steep change definition

The term "steep change" is rather subjective and can be defined as a location between two or more points in the function where the likelihood values experience a significant change. In some cases the likelihood function increases at a slow rate. The algorithm design accounts for this issue by calculating the difference between likelihood values in steps over several values and comparing the results to two thresholds. The difference equation is given by:

$$h(t) = f(z - wt) - f(z - w(t+1)), \quad t = 0, \dots, N \quad (5)$$

where  $f$  is the likelihood function,  $z$  is the maximum intensity,  $w$  is the width of the interval over which the likelihood differences are calculated (e.g. - for  $w=7$  differences are calculated every 7 points), and  $N$  is the total number of points in the searchable area divided by  $w$ . If the calculation in question yields a value greater than or equal to a given threshold, then the intensity corresponding to this location is considered to be a steep change location. The threshold algorithm occurs as follows:

If  $(h(t)_{ML} \geq ML_{T1}); t=0, \dots, m$

Then choice 1 = intensity where that condition is satisfied

If  $(h(t)_{ML} \geq ML_{T2}); t=m, \dots, z$

Then choice 2 = intensity where that condition is satisfied

where  $h(t)_{ML}$  is the steep change value given by equation (5),  $ML_{T1}$  and  $ML_{T2}$  are pre-defined threshold values,  $m$  is the location in the function where the choice 1 condition is satisfied, and  $z$  is the location in the function where the choice 2 condition is satisfied. Once the condition is satisfied for the first threshold value ( $ML_{T1}$ ) then its corresponding intensity value is used to produce the segmentation contour for the first steep change location. Once the condition is satisfied for  $ML_{T2}$  then its corresponding intensity value is used to produce the segmentation contour for the second steep change location.

## 2.5 Validation

The segmentation method was validated on the basis of overlap and accuracy [8,10]:

$$\text{Overlap} = \frac{N_{TP}}{N_{FN} + N_{TP} + N_{FP}} \quad (6)$$

$$Accuracy = \frac{N_{TP} + N_{TN}}{N_{TP} + N_{TN} + N_{FP} + N_{FN}} \quad (7)$$

where  $N_{TP}$  is the true positive fraction,  $N_{TN}$  true negative fraction,  $N_{FP}$  is the false positive fraction, and  $N_{FN}$  is the false negative fraction. The gold standards used for the validation study were mass contours, which have been traced by expert radiologists.

Our experiments produced contours for the intensity values resulting from three locations within the likelihood functions: (1) The intensity for which a value within the likelihood function is maximum (group 1 contour) (2) The intensity for which the likelihood function experiences its first steep change (group 2 contour) and (3) The intensity for which the likelihood function experiences its second steep change (group 3 contour). We have observed that the intensity for which the likelihood function experiences its first steep change produces the contour trace that is most highly correlated with the gold standard traces, regarding overlap and accuracy.

### 3. EXPERIMENTS AND RESULTS

Here we describe the database used, describe the experiments, provide visual results obtained by the algorithm, as well as report the results obtained by the ANOVA test.

#### 3.1 Database

For this study, a total of 122 masses were chosen from the University of South Florida's Digital Database for Screening Mammography (DDSM) [3]. The films were digitized at resolutions of 43.5 or 50  $\mu$ m's using either the Howtek or Lumisys digitizers, respectively. The DDSM cases have been ranked by expert radiologists on a scale from 1 to 5, where 1 represents the most subtle masses and 5 represents the most obvious masses. The images were of varying subtlety ratings. The first set of expert traces was provided by an attending physician of the GUMC, and is hereafter referred to as the Expert A traces. The second set of expert traces was provided by the DDSM, and is hereafter referred to as the Expert B traces.

#### 3.2 Experiments and Results

As mentioned previously, the term "steep change" is very subjective and therefore a set of thresholds needed to be set in an effort to define a particular location within the likelihood function as a "steep change location". For this study the following thresholds were experimentally chosen:  $ML_{T1}=1800$ ,  $ML_{T2}=1300$ , where  $ML_{T1}$ = threshold for steep change location 1 for the likelihood function, and  $ML_{T2}$  = threshold for steep change location 2 for the likelihood function. We performed a number of experiments in an effort to prove that the intensity for which the likelihood function experiences the first steep change location produces the contour trace, which is most highly correlated with the gold standard traces regarding overlap and accuracy.

First we present segmentation results for two malignant cases followed segmentation results for two benign cases. Each figure contains an original image, traces for Experts A and B, and computer segmentation results for groups 1, 2, and 3. Second, we present data that plots the mean values for various margin groups for both overlap and accuracy measurements. The plots

present data for the spiculated and ill-defined groups of malignant masses, and ill-defined and circumscribed groups of benign masses. Data was not presented for the other categories because there was not a sufficient amount of cases.

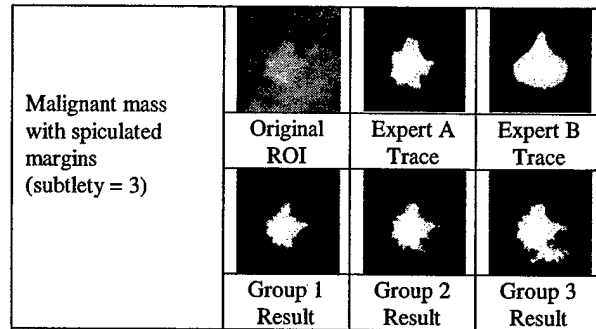


Figure 2: Segmentation Results: Spiculated Malignant Mass

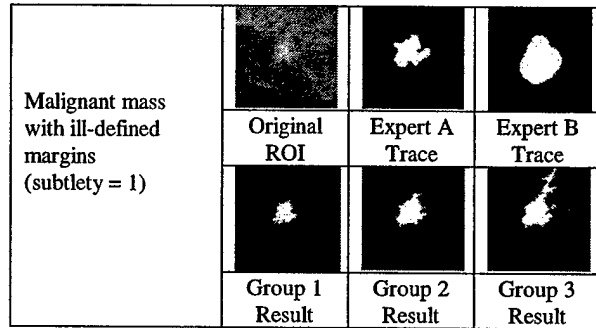


Figure 3: Segmentation Results: Ill-defined Malignant Mass

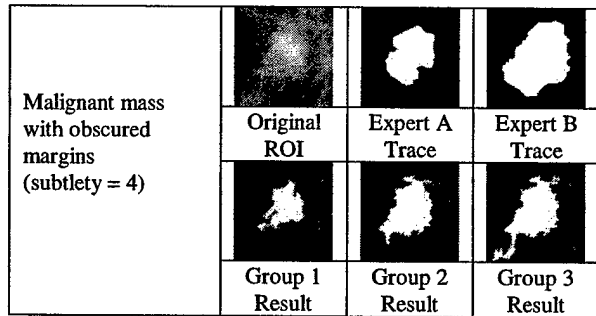


Figure 4: Segmentation Results: Obscured Malignant Mass

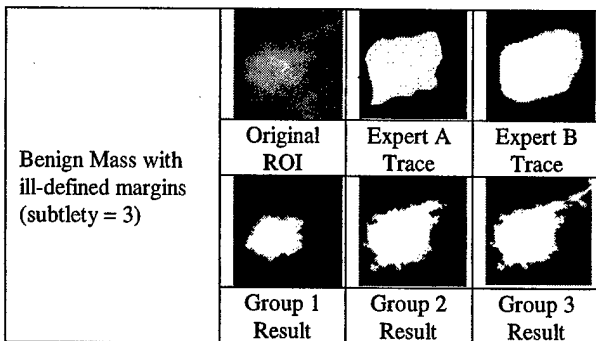


Figure 5: Segmentation Results: Ill-defined Benign Mass

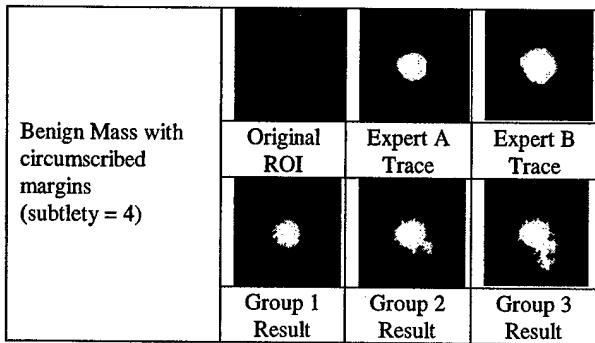


Figure 6: Segmentation Results: Circumscribed Benign Mass

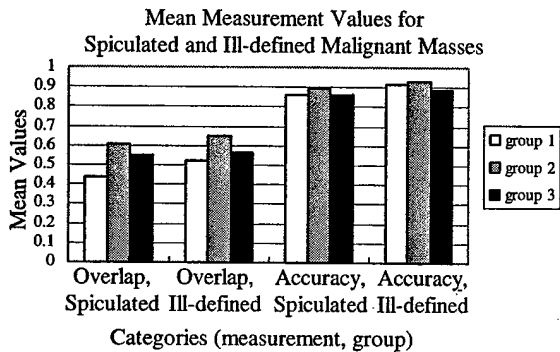


Figure 7: Mean Measurement Values (Malignant Masses)

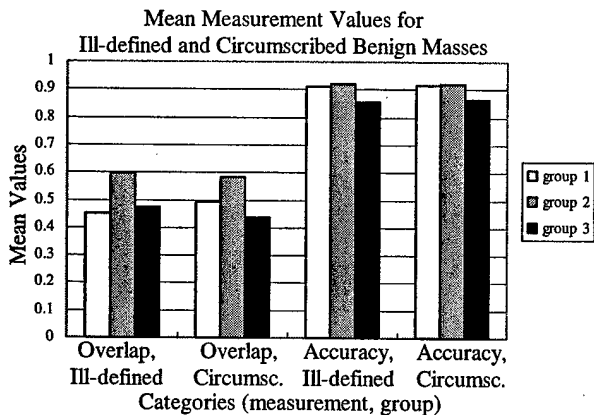


Figure 8: Mean Measurement Values (Benign Masses)

#### 4. DISCUSSION AND CONCLUSION

The visual results (see Figures 2-6) reveal that the group 2 trace appears to delineate the masses better than the group 1 and group 3 contours in most cases. Visually, it appears that the method has performed equally well on all margin groups. This is an encouraging result because some of the more difficult masses to segment are typically those that are spiculated, obscured, and those that have ill-defined borders. The plots shown in Figures 7-8 confirm that the group 2 trace performs better than the other

groups on the basis of overlap and accuracy for all margin groups, therefore supporting our visual observations.

In future work, a worthwhile study would be to test gather more data for all margin groups in an effort to see if the various groups require different parameter values to maximize the algorithm's robustness. Our ultimate goal is to optimize its performance for those masses falling in the ill-defined and obscured margin groups because segmentation of masses falling into those categories is exceedingly difficult.

#### 5. REFERENCES

- [1] M.L. Comer, E.J. Delp, "The EM/MPM algorithm for segmentation of textured images: Analysis and further experimental results", *Proceedings of the 1995 IEEE ICIP*, Lausanne, Switzerland, September 16-19, 1996.
- [2] J.R. Harris, M.E. Lippman, M. Morrow, S. Hellman, "Diseases of the breast", Lippincott-Raven Publishers, Philadelphia, PA, pp. 80-81, 1996.
- [3] M. Heath, K.W. Bowyer, D. Kopans et al., "Current status of the digital database for screening mammography", *Digital Mammography*, Kluwer Academic Publishers, pp. 457-460, 1998.
- [4] M.A. Kupinski, M.L. Giger, "Automated Seeded Lesion Segmentation on Digital Mammograms", *IEEE Trans. on Med. Imag.*, vol. 17, no. 4, pp. 510-517, 1998.
- [5] L. Li, Y. Zheng, L. Zhang, R. Clark, "False-positive reduction in CAD mass detection using a competitive classification strategy", *Med. Phys.*, vol. 28, pp. 250-258, 2001.
- [6] J.E. Martin, "Atlas of mammography: histologic and mammographic correlations (second edition)", Williams and Wilkins, Baltimore, MD, p. 87, 1988.
- [7] N. Petrick, H-P Chan, B. Sahiner, D. Wei, "An Adaptive Density-Weighted Contrast Enhancement Filter for Mammographic Breast Mass Detection", *IEEE Trans. on Med. Imag.*, vol. 15, no. 1, pp. 59-67, 1996.
- [8] J. Suckling, D.R. Dance, E. Moskvic, D.J. Lewis, S.G. Blacker, "Segmentation of mammograms using multiple linked self-organizing neural networks", *Med. Phys.*, vol. 22, pp. 145-152, 1995.
- [9] G.M. te Brake, N. Karssemeijer, "Segmentation of suspicious densities in digital mammograms", *Med. Phys.*, vol. 28, no. 2, pp. 259-266, 2001.
- [10] B. Van Ginneken, "Automatic segmentation of lung fields in chest radiographs", *Med. Phys.*, 27, pp. 2445-2455, 2000.

#### 6. ACKNOWLEDGMENTS

This work was supported by US Army Grant numbers DAMD17-01-1-0267, DAMD 17-00-1-0291, DAAG55-98-1-0187, and DAMD 17-03-1-0314.



## Changes in biophysical parameters of plasma membranes influence cisplatin resistance of sensitive and resistant epidermal carcinoma cells

Xing-Jie Liang,<sup>a</sup> Jun-Jie Yin,<sup>b</sup> Jien-Wei Zhou,<sup>c</sup> Paul C. Wang,<sup>c</sup>  
Barbara Taylor,<sup>a</sup> Carol Cardarelli,<sup>a</sup> Michael Kozar,<sup>d</sup> Raynard Forte,<sup>d</sup>  
Adorjan Aszalos,<sup>a</sup> and Michael M. Gottesman<sup>a,\*</sup>

<sup>a</sup>Laboratory of Cell Biology, National Cancer Institute, National Institutes of Health, Bethesda, MD 20892-4254, USA

<sup>b</sup>Instrumentation and Biophysics Branch, Center for Food Safety and Applied Nutrition, Food and Drug Administration, College Park, MD 20740-3835, USA

<sup>c</sup>Department of Radiology, Howard University, Washington, DC 20060, USA

<sup>d</sup>Division of Experimental Therapeutics, Walter Reed Army Institute of Research, Silver Spring, MD 20910, USA

Received 30 June 2003, revised version received 15 September 2003

### Abstract

The mechanism of resistance of cancer cells to the anticancer drug cisplatin is not fully understood. Using cisplatin-sensitive KB-3-1 and resistant KCP-20 cells, we found that the resistant cells have higher membrane potential, as determined by membrane potential sensing oxonol dye. Electron spin resonance and fluorescence polarization studies revealed that the resistant cells have more “fluid” plasma membranes than the sensitive cells. Because of this observed difference in membrane “fluidity,” we attempted modification of the plasma membrane fluidity by the incorporation of heptadecanoic acid into KB-3-1 and KCP-20 cell membranes. We found that such treatment resulted in increased heptadecanoic acid content and increased fluidity in the plasma membranes of both cell types, and also resulted in increased cisplatin resistance in the KCP-20 cells. This finding is in accord with our results, which showed that the cisplatin-resistant KCP-20 cells have more fluid membranes than the cisplatin-sensitive KB-3-1 cells. It remains to be determined whether the observed differences in biophysical status and/or fatty acid composition alone, or the secondary effect of these differences on the structure or function of some transmembrane protein(s), is the reason for increased cisplatin resistance.

© 2003 Elsevier Inc. All rights reserved.

**Keywords:** Cisplatin resistance; Heptadecanoic acid; Plasma membrane fluidity; Membrane potential; Fluorescence polarization; Human epidermal carcinoma KB cells

### Introduction

Cis-diamminodichloroplatinum II (cisplatin) is one of the most useful anticancer drugs. Treatment protocols for solid tumors of the esophagus, bladder, ovary, testes, head, and neck include this drug. As for most antitumor agents, resistance develops in cancer cells, limiting their efficacy. The reason for resistance against cisplatin is not fully understood. Several mechanisms have been suggested, including decreased cisplatin accumulation [1,2], and alter-

ation of apoptotic signaling [3,4]. Reports also indicate that alterations in growth regulating proteins, such as c-Myc [5], inhibition of caspase-9 [6], and reduced inhibition of DNA synthesis [7] are associated with cisplatin resistance. Involvement of plasma membrane lipids in cisplatin resistance has also been implicated [8]. Britz et al. [9] succeeded in decreasing cisplatin resistance by treating monoclonal cells with a free or liposome-encapsulated bile acid derivative.

Our interest was focused on the biophysical status of plasma membranes in relation to cisplatin resistance. We investigated the biophysical differences between cisplatin-resistant and -sensitive cells and the influence of a fatty acid inserted into the plasma membranes on cisplatin sensitivity of human epidermal carcinoma KB cells.

\* Corresponding author. Laboratory of Cell Biology, Center for Cancer Research, National Cancer Institute, National Institutes of Health, Room 1A-09, 37 Convent Drive, Bethesda, MD 20892-4254. Fax: +1-301-402-0450.  
E-mail address: [mgottesman@nih.gov](mailto:mgottesman@nih.gov) (M.M. Gottesman).

## Materials and methods

### Cell lines

The KB-3-1 cell line was derived from a single clone of human KB epidermal carcinoma cells (a HeLa subclone), after two subclonings, as described by Akiyama et al. [10]. The cisplatin-resistant subline of KB-3-1 cells was selected by exposure to 0.5  $\mu\text{g}/\text{ml}$  cisplatin (KB-CP.5) for 42 days. After that, single clones were picked and propagated in medium containing 0.5  $\mu\text{g}/\text{ml}$  cisplatin. One other cisplatin-resistant cell line, KCP-20, was obtained after 6 months' exposure of KB-3-1 cells to increasing concentrations of cisplatin, up to 20  $\mu\text{g}/\text{ml}$  [11]. KCP-20 cells were maintained in medium containing 5  $\mu\text{g}/\text{ml}$  cisplatin and taken out of cisplatin before making the measurements. All cell lines were grown in Dulbecco's modified Eagle medium (Invitrogen, Grand Island, NY), supplemented with L-glutamine, penicillin, streptomycin (Quality Biological, Gaithersburg, MD), and 10% fetal bovine serum (Whittaker Bioproducts, Walkersville, MD).

### Membrane potential measurements

Membrane potential measurements were performed by flow cytometry, using the negatively charged DiBaC4 (3) oxonol dye (Molecular Probes, Eugene, OR), essentially as described earlier [12]. Briefly, a cell suspension of  $1 \times 10^6$  cells/ml was equilibrated for 1 min in PBS followed by the addition of oxonol dye, 150 M. After exactly 2 min equilibration at room temperature, histograms were collected from  $10^4$  cells. Reproducibility was determined by measuring membrane potentials of the cells on different days, from separate cultures, and by comparing the relative fluorescence of the oxonol-stained cell types.

Oxonol fluorescence intensity measures membrane potential when the extracellular potassium concentration is changed from 5 to 150 mM, resulting in increased fluorescence intensity of the oxonol-stained cells and thus making the cells depolarized. All measurements were made with a Becton Dickinson FACSCalibur flow cytometer (Becton Dickinson, Mountain View, CA), operated with a 15-mW argon ion laser tuned to 488-nm excitation wavelength. Fluorescence emission was collected at 525 nm. Results are expressed in comparative histograms of representative series.

### Polarity of fluorescent membrane probes in live cells

Measurements of steady-state fluorescence polarization were done with a spectrofluorometer LS50B (Perkin Elmer, Norwalk, CT) and the lipid-soluble fluorophore, 1-(4-trimethylammoniumphenyl)-6-phenyl-1,3,5-hexatriene (TMA-DPH) (Molecular Probes). This fluorophore is known to probe plasma membranes of cells at the surface. TMA-DPH was dissolved in tetrahydrofuran at a concentration of 2 mM and was kept in the dark at 4°C. Cells ( $10^6/\text{ml}$ ) were

labeled with TMA-DPH at a concentration of 2  $\mu\text{M}$  in PBS. After 10 min incubation time at 4°C, the cell suspension was centrifuged and washed two times in the centrifuge with PBS. After resuspension in PBS, fluorescence anisotropy was measured at 25°C. The excitation wavelength was 355 nm and the emission was measured at 430 nm with a slit width of 5. Polarization values were calculated according to Collins and Scott [13] by the equation  $P = (I_{0,0} - G * I_{0,90}) / (I_{0,0} + G * I_{0,90})$  from the measured fluorescence intensities.

### Electron spin resonance (ESR) studies on live cells

ESR studies were conducted with 5-doxyl stearic acid (5-doxyl-SA) and with 2,2,6,6-tetramethyl piperidin-1-oxyl-4-yl-octadecenoate (T-SASL) probes (Molecular Probes). The first probe intercalates to the 5 carbon depth in the outer leaflet of the plasma membrane [14] and T-SASL at the surface of the plasma membranes [15]. Labeling the cells with the spin probes was done as follows: 5-doxyl-SA was dissolved in ethanol, 1 mg/ml, and was kept at 4°C. Then,  $1 \times 10^7$  cells were mixed with  $8 \times 10^{-8}$  mol spin label in 0.02 ml volume of PBS. After 1 min contact time, the cell suspension was transferred into a 50- $\mu\text{l}$  micropipette capillary tube and sealed at the bottom with Critoseal (Syva Co., Palo Alto, CA). The micropipette with the cells was placed into the cavity of a Varian E-9 Century series spectrometer (Syva Co.). ESR spectra were recorded at X-band, at 9.5 kHz, 100-field modulation, 4-Gauss modulation amplitude, 100-Gauss sweep range, and at 10 mW microwave power. The temperature of the probe was set to 24°C by the variable temperature accessory using N<sub>2</sub> gas flow. Evaluation of the obtained ESR spectra, when 5-doxyl-SA was used, was by the equation expressing the order parameter  $S$ :

$$S = 0.5407 (T_{11} - T_1) / a_0, \text{ where } a_0 = (T_{11} + 2T_1) / 3$$

and  $T_{11}$  and  $T_1$  are the outer and inner tensors obtained from the ESR spectra.

When the T-SASL probe was used, the same instrument parameters were applied, except that the incident microwave power was 20 mW. The spectral parameters,  $h_0$  and  $h_{-1}$  are the spectral amplitudes and the ratio  $h_0/h_{-1}$  defines the motional freedom of the probe according to Yin et al. [15]. With both spin labels, the ESR spectra show contribution from spin labels of restricted motion with no contribution from the free-moving spin label.

### Lipid packing of plasma membranes in live cells

Plasma membrane lipid packing can be studied by inserting the fluorescence probe merocyanine 540 (MRC 540) (Molecular Probes) into cell membranes and assessing the degree of insertion by fluorescence intensity measurement, using flow cytometry [16,17]. The experiment was according to Schlegel et al. [16] with some modifications. Briefly,  $1 \times 10^7$  cells, suspended in 1 ml of PBS were treated with 10  $\mu\text{l}$  of

a MC540 stock solution of 1 mg/ml, in 60% ethanol, 40% water. After a 10-min incubation at room temperature, cells were pelleted in a centrifuge, washed once in PBS by centrifugation, resuspended in 1 ml PBS, and fluorescence histograms were obtained. A Becton Dickinson FACSCalibur flow cytometer (Becton Dickinson, Franklin Lakes, NJ) was used at 488-nm excitation and 575-nm emission wavelength. Histograms were collected with  $10^4$  cells. Results are expressed as means of fluorescence of the histograms obtained from duplicate measurements of one typical set of cells.

#### *Preparation of cells for NMR spectrometry*

KB-3-1 and KCP-20 cells were grown to 90% confluence, harvested with 0.05% trypsin, 0.53  $\mu$ M EDTA, centrifuged at 4°C at  $730 \times g$  for 10 min, and washed twice with growth medium. To perform a long-term NMR study, the cells were restrained in an agarose thread [18,19]; 0.5 ml of ( $9 \times 10^7$  cells) was mixed with an equal volume of liquid agarose in phosphate-buffered saline, and immersed in a bath at 37°C for 5–7 min. The mixture was extruded under low pressure through cooled tubing (0.5 mm ID) into a 10-mm NMR tube containing growth medium. Using 0.5-mm threads ensures that there is no metabolic compromise, and the cells are viable and in stable energetic status for a long period of time, while the threads maintain their mechanical strength. The gel threads, which fill the tube, are concentrated without compression at the bottom of the NMR tube by insertion of a plastic insert with the perfusion fitting. A Teflon inflow tube (0.5 mm ID) was placed near the bottom of the tube. The gel threads were perfused with growth medium at 0.9 ml/min. Cells were continuously perfused for more than 40 h. Accumulation of data was started within 30 min after the harvest.

#### *NMR spectrometry of live cells*

The  $^{31}\text{P}$  NMR spectra were recorded at 37°C on a Varian XL-400 machine (Varian Associates, Inc., Palo Alto, CA) at 162 MHz using RF pulse corresponding to a 72° flip angle and 2 s repetition time. The flip angle used was the Ernst angle for phosphocreatine (PCr) (T1 relaxation time, 3 s). There were more than 40 spectra obtained. Each spectrum contained 1800 transients and took 1 h. During the entire study, the system was deuterium locked with an external source (99.9%  $\text{D}_2\text{O}$  in a capillary, Sigma, St. Louis, MO) to avoid magnetic field drift.

All the spectra were transformed and viewed separately to confirm that the spectra did not change during the experiment. There were 25,000 data points collected and zero-filled to 8k before Fourier transformation. The spectra were added and 10-Hz line broadening was applied to obtain Fig. 3. The chemical shifts were standardized to  $\beta$ -adenosinetriphosphate ( $\beta$ -ATP) set to  $-18.70$  ppm. Many phosphorus metabolites were identified, including phosphocholine (PC,

3.57 ppm), inorganic phosphate (Pi, 2.59 ppm), glycerophosphoethanolamine (GPE, 0.81 ppm), glycerophosphocholine (GPC, 0.26 ppm), phosphocreatine (PCr,  $-2.69$  ppm),  $\gamma$ -adenosine triphosphate ( $\gamma$ -ATP,  $-5.12$  ppm),  $\alpha$ -adenosine triphosphate ( $\alpha$ -ATP,  $-10.19$  ppm), and diphosphodiester (dPdE,  $-10.86$ ,  $-12.58$  ppm). Chemical shifts of these molecules are also listed in the literature [18,19].

#### *Treatment of cells with heptadecanoic acid and cell proliferation studies*

Treatment of KB-3-1 and KCP-20 cells with heptadecanoic acid was carried out in 24-well plates (Corning Inc., Corning, NY), with modification of the method used by Callaghan et al. [20]. After exploratory dose selection studies for cisplatin and heptadecanoic acid, the final conditions were as follows: cells ( $10^6$ /ml) were incubated in appropriate medium, as described above for both cell types, and after 2–3 days of incubation, the medium was withdrawn and replaced by serum-free medium. Following 6 h incubation at 37°C, 5%  $\text{CO}_2$  medium was replaced by serum-free medium containing different concentrations of heptadecanoic acid or nothing. This incubation was followed by replacement of the medium with complete medium containing cisplatin or nothing. KB-3-1 cells were treated with 0.08  $\mu$ g/ml and KCP-20 cells with 5  $\mu$ g/ml cisplatin from a stock solution of 500  $\mu$ g/ml aqueous solution. Cells were harvested after 5–6 days' incubation and treated with heptadecanoic acid alone, with cisplatin alone, heptadecanoic acid plus cisplatin or nothing, and were counted after trypsinization by a Coulter Particle Counter (Coulter Electronics, Luton, UK). Calculation of proliferation was based on cells treated with nothing as 100%. The expected yield was: cell count of cells treated with heptadecanoic acid alone multiplied by cell count of cells treated with cisplatin alone. The cell count of cells treated with both reagents was then related to the previous cell count product and tabulated.

#### *Preparation of plasma membranes for determination of relative fatty acid composition*

For the purpose of plasma membrane preparation,  $10^7$  cells from each cell line were harvested at log phase and washed with ice-cold PBS. Cells were sedimented by centrifugation and then suspended in ice-cold hypotonic solution (0.5 mM  $\text{KH}_2\text{PO}_4$ , 0.1 mM EDTA containing 1% protease inhibitor aprotinin, pH 8.0) for 5 min. Cells were disrupted on ice by a tight Dounce homogenizer with constant 40 strokes. Samples were checked for complete disruption in a phase-contrast microscope. Homogenates were centrifuged at  $2000 \times g$  for 10 min at 4°C to discard the nuclei and then the supernatant was centrifuged at  $25,000 \times g$  for 25 min to pellet all other organelles. The resulting supernatant was further centrifuged for 55 min at 4°C. The membranes sedimented at the bottom and were stored at  $-80^\circ\text{C}$  before fatty acid analysis. To determine

that the sediment contained only plasma membranes and no membranes of organelles, markers were used in connection with Western blot analyses. For a positive marker, the anti-integrin antibody anti-2/VLA-2 $\alpha$  was used according to Emsley et al. [21].

#### *Conversion of plasma membrane lipids to methyl esters and fatty acid analysis*

Fats were extracted into organic phase by vortexing the membrane preparations obtained as described above, with minor modification of the methods of Kozar et al. [22]. In brief, 2 ml of HPLC-grade water (Fisher Scientific, Pittsburgh, PA) was added to the membranes together with 3.75 ml of 2:1 (v/v) methanol/chloroform (Fisher Scientific) and the suspension was vortexed for 15 min. Then, after addition of 1 ml chloroform and 1 min vortexing, the suspension was centrifuged for 10 min at 2000 rpm. The separated organic phase was dried in an N<sub>2</sub> stream and heated in 1 ml 2 M methanolic HCl [11 ml methanol with dropwise addition of 2.5 ml acetyl chloride (Sigma)] at 85°C for 18 h in a screw-capped tube. The fatty acid methyl esters which formed were then extracted into heptane for GC-MS analysis. Samples were analyzed on a Hewlett-Packard 6890 plus GC equipped with 7683 auto-injector. The injection port was held at constant 280°C with 2  $\mu$ l injected in the splitless mode onto a DB-5 ms capillary column with 30 m  $\times$  0.25 mm ID  $\times$  0.25  $\mu$ m film thickness (J&W Scientific, Folsom, CA). Initial oven temperature was 80°C with a ramp of 40°C/min to a final temperature of 290°C and hold for 0.75 min. Helium was used as the carrier gas at a constant velocity of 41 cm/s. Electron impact ionization at 70 eV was performed using standard autotune conditions. The source temperature was maintained at 230°C while the quadrupoles were maintained at 150°C. FAMES were analyzed in full scan mode for qualitative identification as well as in selected ion monitoring mode for ratio determination. Location of the analyzed two fatty acids in the obtained chromatograms was ascertained by standards of hexa- and heptadecanoic acid methyl esters (Sigma). The ratio of heptadecanoic acid to hexadecanoic acid methyl esters was determined since heptadecanoic acid was used to treat the cells and the hexadecanoic acid content of cells was assumed to be constant. This ratio is defined as the area under the peak for hexadecanoic acid/area under the peak for heptadecanoic acid methyl esters.

#### *Visualization of distribution of K<sup>+</sup> channels in cells by immunofluorescence microscopy*

For visualization of distribution of K<sup>+</sup> channels in cells, cells were grown on 189-mm glass coverslips in petri dishes. Cells were fixed with 3.5% formaldehyde in PBS for 10 min, followed by 0.1% Triton X-100 treatment for 5 min for permeabilization. After washing, cells were treated with 3% BSA in PBS for 30 min and subsequently treated with the primary antibody (Ab) for 1 h. The Ab was TWIK-

2 (P-19) goat polyclonal Ab (Santa Cruz Biotechnology, Santa Cruz, CA). After five washings, cells were incubated with Cy<sup>TM</sup>3-conjugated affinity pure donkey anti-goat, secondary Ab (1:100 dilution) (Jackson Immuno-research Laboratory). Cells were washed extensively after the secondary Ab treatment. The slides with the treated cells were mounted on microscope slides with fluorescence mounting medium (Dako, Carpinteria, CA). Background fluorescence was determined from cells treated only with the secondary Ab, but otherwise treated the same way as described with the primary Ab. Fluorescent images were collected with a Bio-Rad 1024 confocal scan head mounted on a Nikon Optiphot microscope with a 60 $\times$  planapochromat lens. Excitation at 568 nm was provided by a krypton-argon gas laser. An emission filter of 598/40 was used for collecting red fluorescence in channel one and phase contrast images of the same cell were collected in another channel using a transmitted light detector.

## Results

#### *Membrane potential of cisplatin-sensitive and -resistant cells*

Membrane potential was measured using several series of independently grown cell cultures. For each measurement at different times and with the different cell lines, we observed the same pattern of membrane potentials. Fig. 1 shows one typical result of several measurements with the series of the cells. The KCP-20 cells, which are highly resistant to cisplatin, had lower fluorescence intensities and thus are hyperpolarized as compared to cisplatin sensitive and single-step, low-level resistant cells (KB-CP.5). Oxonol is a negatively charged membrane potential sensing dye and therefore less dye diffuses into membranes of cells which are more negative, and thus are hyperpolarized.

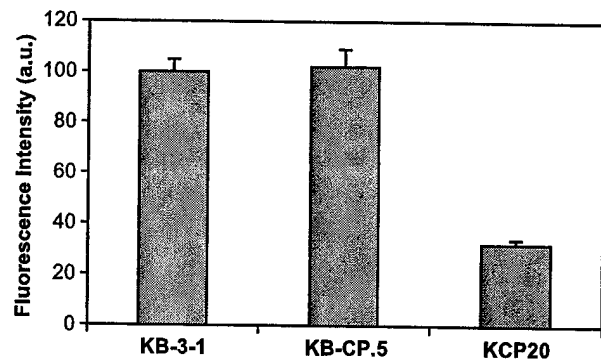


Fig. 1. Relative membrane potential of cisplatin-sensitive KB-3-1 and -resistant cells is indicated by the fluorescence of oxonol (150 mM)-stained cells. Oxonol is a negatively charged membrane potential sensing dye and was used as detailed in Materials and methods. One typical series of measurement of cells were grown simultaneously in culture ( $n = 2-3$ ).  $P < 0.05$  between KB-3-1 and KCP-20 cells. No statistical difference exists between KB-3-1 and KB-CP.5 cells.

### Polarity of the fluorescent TMA-DPH molecule in the plasma membrane of live cells

The TMA-DPH fluorescence probe was used to measure the fluidity of plasma membranes because it has been shown that this probe does not penetrate into the cells and probes at the upper leaflet of the membrane [13]. Table 1 shows the results obtained with sensitive KB-3-1 and resistant KB-20 cells treated or not treated with heptadecanoic acid. Cisplatin-resistant KCP-20 cells were found to have membranes which were more fluid; the calculated polarization number,  $P$ , was of lower value. These results parallel those obtained with ESR measurements (see below). Also, polarization numbers obtained with the TMA-DPH probe indicate that heptadecanoic acid treatment of the cells results in lower polarization numbers. Therefore, the plasma membranes become more fluid. These results also parallel those obtained by ESR measurements (see below).

### ESR studies on the motional freedom of ESR probes, 5-doxyl-SA and T-SASL, in the plasma membranes of cells

Two ESR probes were used to measure membrane fluidity in cisplatin-sensitive KB-3-1 and -resistant KCP-20 cells. 5-doxyl-SA probes at 5 carbon depth in the outer leaflet, while the T-SASL probes at the surface of the plasma membrane [14,15]. Table 2 shows both results. The calculated order parameters,  $S$ , for the 5-doxyl-SA yielded lower numbers for the cisplatin-resistant KCP-20 cells, indicating more “fluid” membranes of these cells at 24°C. The calculated  $h_0/h_{-1}$  parameters also indicate a more fluid membrane for the cisplatin-resistant KCP-20 cells. These results are in line with those of the polarization experiments.

To measure membrane fluidity changes of heptadecanoic acid treated KB-3-1 and KCP-20 cells, we employed the 5-doxyl-SA ESR probe. Fig. 2 shows the results and indicates that both types of cells became more fluid (had lower  $S$  values) after heptadecanoic acid treatment. The heptadecanoic acid-treated KCP-20 cells were shown to be more resistant than the nontreated KCP-20 cells. This result is consistent with the fact that the cisplatin-resistant KCP-20

Table 1  
Polarity<sup>a</sup> of TMA-DPH fluorescence probe, inserted into plasma membranes of heptadecanoic acid<sup>b</sup>-treated and untreated cisplatin-sensitive (KB-3-1) and -resistant (KCP-20) cells

Cells/treatment	Polarity	±SD
KB-3-1 untreated	0.3668	0.0018
KB-3-1 treated	0.3590	0.0013
KCP-20 untreated	0.3612	0.0018
KCP-20 treated	0.3556	0.0016

<sup>a</sup> Mean polarization numbers are calculated from six independent measurements.

<sup>b</sup> Heptadecanoic acid treatment is detailed in Materials and methods. Heptadecanoic acid (40 μM) was used in each experiment.  $P < 0.05$  between treated and untreated cells as well as between KB-3-1 and KCP-20 cells.

Table 2

Motional freedom<sup>a</sup> of 5-doxyl-SA and T-SASL ESR probes inserted into the plasma membranes of cisplatin-sensitive and -resistant cells

Cells	Temp, °C	5-doxyl-SA, order parameter, $S$		T-SASL, $h_0/h_{-1}$	
		$S$	±SD	$h_0/h_{-1}$	±SD
KB-3-1	24	0.6443	0.0038	2.423	0.093
KCP-20	24	0.6208	0.0111	1.820	0.147

<sup>a</sup> Order parameter,  $S$ , and  $h_0/h_{-1}$  were calculated as described in Materials and methods. Experiments were done with several cultures ( $n = 2-4$ ), and ESR measurements were in triplicate;  $P < 0.05$ .

cells were found to have more fluid plasma membranes than the sensitive KB-3-1 cells by both ESR and polarization techniques (Tables 1 and 2). Contrary to this, the cisplatin-sensitive KB-3-1 cells became even more sensitive after heptadecanoic acid treatment, despite the fact that their plasma membranes became more fluid after this treatment (data not shown).

### Membrane packing as determined by fluorescence intensity of merocyanine 540-stained cells

Merocyanine (MRC) 540 staining was found to be indicative of the lipid packing density of cell plasma membranes [16]. We applied this measurement to cisplatin-sensitive KB-3-1 and -resistant KCP-20 cells as detailed in Materials and methods, and found that cisplatin resistant cells had lower fluorescence intensity than the sensitive KB-3-1 cells. The fluorescence intensity of merocyanine540-stained KB-3-1 cells was  $95 \pm 10$  while that of the resistant KCP-20 cells was  $58 \pm 12$  in a typical cell preparation ( $n = 3$ ). We interpret these results to mean that in KB-3-1 cell membrane lipids are more tightly packed and intercalate MRC 540 more tightly than in KCP-20 cells. These results parallel those of membrane fluidity measurements by the polarization and ESR methods (Tables 1 and 2).

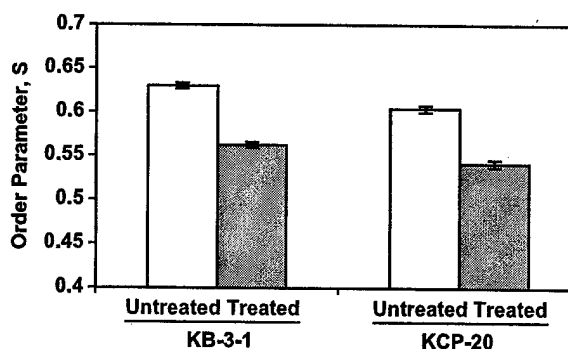


Fig. 2. Membrane “fluidity” as expressed by the order parameter,  $S$ , of cisplatin-sensitive KB-3-1 and -resistant KCP-20 cells, treated or not treated with heptadecanoic acid. Order parameters,  $S$ , were calculated from ESR spectra obtained as described in Materials and methods. Heptadecanoic acid treatment is also described in Materials and methods. Average of three to four measurements are shown with SDs. There is a statistically significant difference between  $S$  values of heptadecanoic acid treated and untreated cells for both types of cells ( $P < 0.05$ ).

### Assessment of phospholipids in cisplatin-sensitive KB-3-1 and -resistant KCP-20 cells by $^{31}\text{P}$ NMR spectrometry

Spectra obtained by 400-MHz NMR spectrometry were compared to detect any difference in phospholipid composition between cisplatin-sensitive KB-3-1 and -resistant KCP-20 cells. The two cell line types were grown in the same media, harvested before confluence, and spectra were obtained as described in Materials and methods. Similar experiments have been performed for the detection of such differences between P-glycoprotein expressing and nonexpressing cells [23,24]. Spectra from both cells detected phospho-ethanolamine, 4.11 ppm; -choline, 3.6 ppm; -creatine, -2.69 ppm; glycerophosphoethanolamine, 0.7 ppm, and choline, 0.1 ppm, besides inorganic phosphate and different adenosinetriphosphates (Fig. 3). No significant differences could be detected between the two cell lines in the above listed phospholipid signals with the applied NMR technique.

### Cell proliferation of heptadecanoic acid-treated and untreated cells

Cell proliferation studies were done as described in Materials and methods. Relative cell counts are shown in Table 3. Results indicate that heptadecanoic acid treatment increased resistance of the KCP-20 cells to cisplatin, since

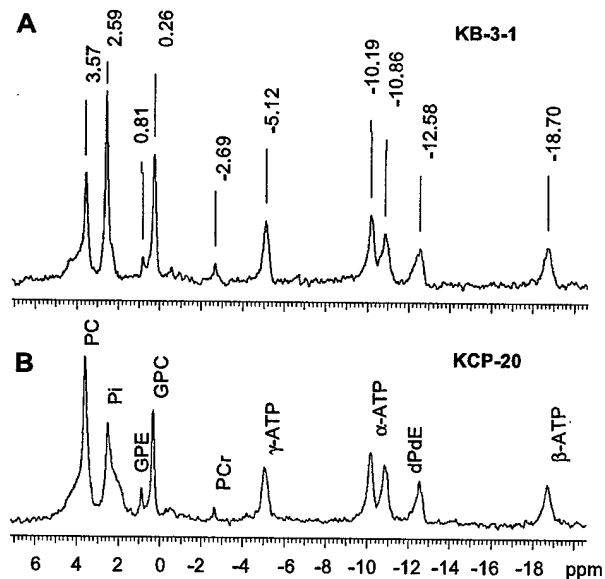


Fig. 3.  $^{31}\text{P}$  NMR spectra (400 MHz) of cisplatin-sensitive KB-3-1 (A) and -resistant KCP-20 (B) cells. Cells ( $9 \times 10^7$ ) from each culture were embedded in agarose and packed in 10-mm NMR tubes. Many water-soluble phosphates were identified, including phosphocholine (PC, 3.57 ppm), inorganic phosphate (Pi, 2.59 ppm), glycerophosphoethanolamine (GPE, 0.81 ppm), glycerophosphocholine (GPC, 0.26 ppm), phosphocreatine (PCr, -2.69 ppm),  $\gamma$ -adenosine triphosphate ( $\gamma$ -ATP, -5.12 ppm),  $\alpha$ -adenosine triphosphate ( $\alpha$ -ATP, -10.19 ppm), diphosphodiester (dPdE, -10.86 ppm, -12.58 ppm), and  $\beta$ -adenosinetriphosphate ( $\beta$ -ATP, -18.70 ppm).

Table 3

Cell proliferation as expressed in percentage  $\pm$  SD cell growth relative to nontreated KB-3-1 and KCP-20 cells in the presence and absence of treatment with heptadecanoic acid or cisplatin or the combination of both

Cells	Treatment	% Proliferation	
		Expected	Found
KB-3-1	[a] cisplatin (0.8 $\mu\text{g}/\text{ml}$ )	–	85 $\pm$ 6
	[b] HAD <sup>a</sup> (20 $\mu\text{M}$ )	–	97 $\pm$ 3
	[c] HDA (40 $\mu\text{M}$ )	–	94 $\pm$ 4
	[a] $\times$ [b]	82 $\pm$ 8	49 $\pm$ 15
	[a] $\times$ [c]	80 $\pm$ 10	68 $\pm$ 12
KCP-20 <sup>b</sup>	[d] cisplatin (5 $\mu\text{g}/\text{ml}$ )	–	67 $\pm$ 10
	[e] HDA (40 $\mu\text{M}$ )	–	68 $\pm$ 5
	[f] HDA (50 $\mu\text{M}$ )	–	41 $\pm$ 11
	[d] $\times$ [e]	45 $\pm$ 14	62 $\pm$ 6
	[d] $\times$ [f]	27 $\pm$ 20	46 $\pm$ 5
	[g] cisplatin (6 $\mu\text{g}/\text{ml}$ )	–	51 $\pm$ 8
	[h] HDA (40 $\mu\text{M}$ )	–	68 $\pm$ 13
	[i] HDA (50 $\mu\text{M}$ )	–	41 $\pm$ 7
	[g] $\times$ [h]	34 $\pm$ 21	47 $\pm$ 5
	[g] $\times$ [i]	19 $\pm$ 19	23 $\pm$ 7

<sup>a</sup> HDA: heptadecanoic acid.

<sup>b</sup> KCP-20 cells: Each measurement of cell growth was done in triplicate wells and each dose was used in multiple experiments with separately grown cell cultures ( $n = 3-5$ ).  $P < 0.05$  for the difference between expected growth and actual growth for all experiments, except for KCP20 cells treated with cisplatin, 6  $\mu\text{g}/\text{ml}$  and 50  $\mu\text{M}$  HDA.

the cells grew better in the combination of cisplatin and heptadecanoic acid than would have been mediated from the growth of these cells in either agent alone. In contrast, heptadecanoic acid treatment of the sensitive KB-3-1 cells increased their sensitivity to cisplatin.

### Fatty acid analysis in heptadecanoic acid-treated and nontreated plasma membranes

Results of the fatty acid analysis are shown in Table 4. Two sets of membrane preparations were made from

Table 4

Area<sup>a</sup> and ratios of area of hexadecanoic and heptadecanoic acids as measured by GC-MS in the membranes of heptadecanoic acid-treated and untreated KB-3-1 and KCP-20 cells

Cells/treatment	Area at $m/z$ 270 heptadecanoic acid <sup>a</sup>	Area at $m/z$ 284 $m/z$ 270/ $m/z$ 284	Ratio of hexadecanoic acid
KB-3-1	5,243,334	65,763	79.73
KB-3-1 + treatment	14,684,547	1,998,304	7.35
KB-3-1	13,859,715	260,720	53.16
KB-3-1 + treatment	15,527,957	1,789,737	8.68
KCP-20	17,554,572	321,183	54.66
KCP-20 + treatment	11,695,325	2,260,349	5.17
KCP-20	6,596,479	122,458	53.87
KCP-20 + treatment	7,656,383	1,332,033	5.75

<sup>a</sup> Area under peaks obtained by GCMS represents fatty acid methyl esters analyzed in full scan mode with the instrument software.

treated and untreated sensitive and resistant cells. For each preparation, Western blot analyses indicated that only plasma membranes were collected (not shown). Results indicated that heptadecanoic acid treatment increased this fatty acid relative concentration to hexadecanoic acid in both cell lines. The hexadecanoic acid content of cell membranes was used to normalize the relative concentration of heptadecanoic acid.

#### Fluorescence visualization of $K^+$ channels in human epidermal carcinoma KB cells

Fig. 4 shows fluorescence images of the KB-3-1 and KCP-20 cells stained with the Cy<sup>TM</sup>3-conjugated affinity pure donkey anti-goat Ab after incubation of the cells with the primary TW1K-2 (P-19) goat polyclonal Ab. The red fluorescence intensities indicate that there are substantially more  $K^+$  channels on the plasma membranes of KCP-20 cells than of KB-3-1 cells.

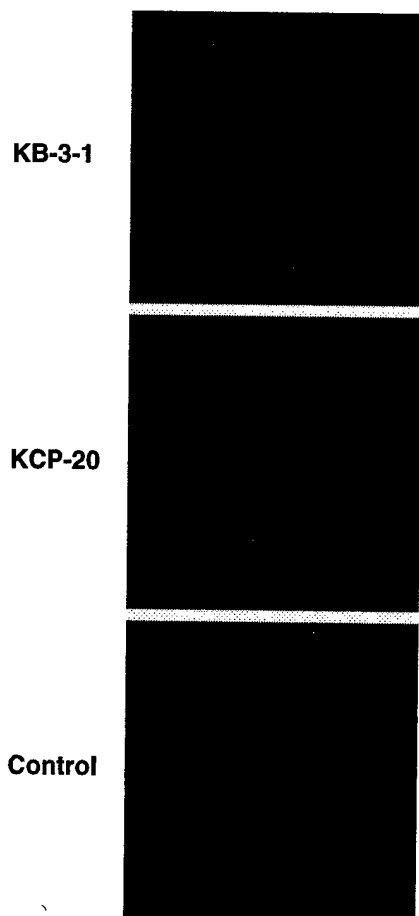


Fig. 4. Confocal visualization of  $K^+$  channels as detected by TW1K-2 primary and Cy<sup>TM</sup>3-conjugated donkey anti-goat secondary Ab. Ab treatment and confocal microscopy are detailed in Materials and methods. Several fields of cells were captured and one representative field of each is shown ( $n = 5-8$ ). Control: KCP-20 cells treated only with secondary Ab.

#### Discussion

We used five different methods to study biophysical differences in the plasma membranes of cisplatin-sensitive KB-3-1 adenocarcinoma cells and their cisplatin-resistant counterparts. We also influenced these biophysical differences in the plasma membranes of KB cells by inserting heptadecanoic acid into the cell membranes. The alteration of lipid composition by addition of heptadecanoic acid resulted in changes in some biophysical parameters of the membranes along with changes in the cells' resistance to cisplatin.

First, we showed that the highly resistant KCP-20 cells have higher membrane potential, and are therefore more hyperpolarized than the sensitive, parental KB-3-1 cells and the low level resistant KCP.5 cells (Fig. 1). We have attributed this increased membrane potential of KCP-20 cells to the increased expression of  $K^+$  channels on their plasma membranes (Fig. 4). Our results are in line with the observation of Thomson et al. [25] that cisplatin treatment of cells influences  $K^+$  channel activity and that of Mahaswari et al. [26] that cisplatin can change ion conductivity in bilayer lipid membranes. Efflux of  $K^+$  from cells can elevate membrane potential. Second, polarization studied with the TMA-DPH fluorescence probe, which probes at the outer leaflet of plasma membranes, indicates that the resistant KCP-20 cells have lower polarization values, and thus have more fluid plasma membranes than the sensitive KB-3-1 cells (Table 1). Third, similar conclusions could be drawn from the ESR studies, performed with two types of ESR probes. Results indicate that the order parameter,  $S$ , and parameters of the measurements with the second probe,  $h_0/h_{-1}$ , are lower for the resistant cells, indicating more fluid membranes for these cells as compared to the sensitive cells (Table 2).

Fourth, more MRC 540 fluorescent dye is packed into the plasma membranes of the sensitive KB-3-1 cells than into the plasma membranes of the resistant KCP-20 cells (see Results). We have interpreted this difference by assuming that more "rigid" membranes can bind more of this dye tightly than the more loosely packed membranes. Both cells are equal in size, so more dye incorporation into a cell cannot be interpreted from different cell sizes. Our interpretation, based on our polarization and ESR measurements done with the same cells with which we performed our MRC 540 lipid packing experiment, is seemingly contrary to the interpretation of Schlegel et al. [16] and Stillwell et al. [17]. However, Schlegel's experiments with lymphocytes could not be interpreted in terms of the ability of MRC 540 to distinguish between loosely or tightly packed membranes. Stillwell found that more MRC 540 dye intercalates into loosely packed membranes of phospholipid vesicles, but he made no such comparison with live cells. His experiments with the T27A leukemia cells demonstrated only that MRC 540 intercalates into docosahexanoic acid modified cells differently than into the nonmodified cells and no interpre-

tation was given for the relationship between membrane fluidity and dye packing. In a previous study [27], MRC 540 intercalated into cisplatin-sensitive and -resistant lung adenocarcinoma cells with the same relative dye ratio as in our study. Unfortunately, no correlation was made between dye packing and membrane fluidity in that study.

We have not detected any significant difference between the 400 MHz  $^{31}\text{P}$  NMR spectra of KB-3-1 and KCP-20 cells (Fig. 3), suggesting that there are no major differences in measured water-soluble phosphates, including phospholipid precursors in the cisplatin-sensitive and -resistant cell lines. Our results reflect relative peak intensities of individual phosphates which depend on their T1 relaxation times and the repetition time (2 s) of the applied NMR technique. Spellman [8] found that phosphatidylserine binds cisplatin *in vitro*, but formation of a phosphatidylserine–cisplatin complex could not be found when experiments were conducted with intact cells [28]. Kaplan et al. [23] found that there are differences in the glycerophosphocholine and glycerophosphoethanolamine ratio in some MCF-7 wild type and P-glycoprotein expressing cell lines by their  $^{31}\text{P}$  NMR studies. However, these differences proved not consistently present in all such cell lines.

We found differences in biophysical parameters between the KB-3-1-sensitive and the KB-20-resistant cells, as described above. Therefore, our next experiment focused on the introduction of biophysical changes to the plasma membrane of the sensitive and the resistant KB cells and determining the cisplatin sensitivity of the altered cells. In a previous study, Callaghan et al. [20] found that the incorporation of heptadecanoic acid into plasma membranes can hinder the function of a transmembrane protein, P-glycoprotein, possibly by altering the biophysical milieu of this transmembrane protein. Therefore, we incorporated this fatty acid into the plasma membrane of KB-3-1 and KCP-20 cells. We demonstrated that during a short treatment period of the cells with this fatty acid, other components of the plasma membrane, such as the cholesterol content, did not change significantly.

After heptadecanoic acid treatment of our cells, we determined changes in membrane biophysical status, relative heptadecanoic acid content, and sensitivity of the treated cells to cisplatin. We found that heptadecanoic acid treatment of the cells increases the relative content of this fatty acid in cell membranes (Table 4). Simultaneously, this treatment increased the fluidity of plasma membranes of both KB-3-1 and KCP-20 cells as measured by polarization (Table 1) and by ESR (Fig. 2). We also measured the influence of heptadecanoic acid treatment on cell proliferation (Table 3). After heptadecanoic acid treatment of KCP-20 cells, their resistance to cisplatin increased (Table 3) and their plasma membrane fluidity increased (Fig. 2). This finding is in accord with our results that the resistant KCP-20 cells have more fluid plasma membranes than the sensitive KB-3-1 cells, as discussed above. That a bile acid derivative increased sensitivity of monoclonal cells to cis-

platin, as reported by Briz et al. [9], is not a direct contradiction to our findings. First, it was not shown by Briz et al. whether the bile acid derivative was incorporated into plasma membranes, and second, no determination was made on the biophysical status of the membranes of the cells before and after the treatment.

Contrary to the results with the KCP-20 cells, KB-3-1 cells became more sensitive to cisplatin after heptadecanoic acid treatment (Table 3). In this case, increasing the fluidity of the plasma membrane did not result in higher resistance to cisplatin, as it did with the KCP-20 cells. Nevertheless, cisplatin sensitivity was altered by heptadecanoic acid treatment in these cells also. Further experiments with cell lines of different plasma membrane fluidity and sensitivity to cisplatin may explain these results. Results detailed above, that incorporation of heptadecanoic acid into plasma membranes of KB-3-1 and KCP-20 cells resulted in opposite sensitivity to cisplatin, indicate that this fatty acid *per se* is not involved in cisplatin binding. Somewhat different results were obtained by Timmer-Bosscha et al. [29] who found that incorporation of docosahexaenoic acid into the membranes of a human small cell lung carcinoma line, GLC4 and its resistant subline, GLC4-CP, decreased resistance of the resistant cells but had no influence on the parent cell line. However, their experimental results suggested that DNA-related effects, and not alteration in the plasma membrane, are the reasons for changes in resistance. Interestingly, these authors also found that their treatment does not cause the same change in cisplatin resistance in the parental as in the resistant cells. Our results parallel this different effect on sensitive and resistant cells. In both cases, this difference suggests that increased fluidity *per se* may not be responsible for cisplatin resistance, but may facilitate a mechanism of resistance found only in the selected cell line.

Recent physiological studies on the mechanism of resistance of KCP-20 cells to cisplatin (and cross-resistance to other compounds such as methotrexate) have revealed the following phenotype: (1) decreased drug accumulation for many drugs associated with decreased expression on the cell membrane of many different transporters, carriers, and channels [11]; (2) neutralization of the usual acidic pH of lysosomes and endosomes [30]; (3) hypermethylation of genes whose expression is decreased in KCP-20 cells (Shen, D.-W., Liang, X.-J., Pai-Panandiker, A., and Gottesman, M.M., unpublished data); and (4) mislocalization of membrane proteins with accumulation of certain transporters in the cytoplasm [31]. Although a single molecular defect is unlikely to account for all of these changes in cells selected in multiple steps, alteration of the biophysical properties of plasma membranes in cisplatin-resistant cells could facilitate defects in membrane protein trafficking which might underlie cisplatin resistance due to decreased accumulation. If increased membrane fluidity amplifies the effect of another defect in KB-CP20 cell membranes, rather than independently causing resistance to cisplatin, this could explain why

measured membrane fluidity in the KB-3-1 parental, drug-sensitive cells does not result in resistance.

To summarize, we have determined that there are differences in biophysical parameters, membrane potential, motional freedom of polarization and ESR probes, and MRC 540 dye packing between cisplatin-sensitive and -resistant human epidermal carcinoma cells *in vitro*.  $^{31}\text{P}$  NMR studies indicated no essential differences in water-soluble phosphates. Modification of the plasma membrane fluidity of these cells by incorporation of heptadecanoic acid resulted in changes in their sensitivity to cisplatin. Whether changes in membrane fluidity transmitted to some membrane molecules in sensitive and resistant cells cause alterations in cisplatin sensitivity remains to be determined.

## References

- [1] Z.S. Chen, M. Mutoh, T. Sumizawa, T. Furukawa, M. Haraguchi, A. Tani, N. Saijo, T. Kondo, S.I. Akiyama, An active efflux system for heavy metals in cisplatin-resistant human KB carcinoma cells, *Exp. Cell Res.* 240 (1998) 312–320.
- [2] M. Bungo, Y. Fujiwara, K. Kasahara, K. Nakagawara, Y. Ohe, Y. Sasaki, S. Irino, N. Saijo, Decreased accumulation as a mechanism of resistance to cis-diamminodichloro platinum (II) in human non-small cell lung cancer cell lines: relation to DNA damage and repair, *Cancer Res.* 50 (1990) 2549–2553.
- [3] H. Burger, K. Nooter, A.W. Boersma, C.J. Kortland, G. Stoter, Expression of p53, Bcl-2 and Bax in cisplatin-induced apoptosis in testicular germ cell tumor cell lines, *Br. J. Cancer* 77 (1998) 1562–1567.
- [4] J. Kigawa, S. Sato, M. Shimada, M. Takahashi, H. Itamochi, Y. Kanamori, N. Terakawa, p53 gene status and chemosensitivity in ovarian cancer, *Hum. Cell* 14 (2001) 165–171.
- [5] S. Adachi, A.J. Obaya, Z. Han, N. Ramos-Desimone, J.H. Wyche, J.M. Sedivy, c-Myc is necessary for DNA damage-induced apoptosis in the G phase of cell cycle, *Mol. Cell Biol.* 21 (2001) 4929–4937.
- [6] D. Kuwahara, K. Tsutsumi, T. Kobayashi, M. Hyoudou, I. Koizuka, Inhibition of caspase-9 activity in cisplatin-resistant head and neck squamous cell carcinoma, *Nippon Jibi Inkoka Gakkai Kaiho* 105 (2002) 152–157.
- [7] S. Lin-Chao, C.C. Chao, Reduced inhibition of DNA synthesis and G(2) arrest during the cell cycle of resistant HeLa cells in response to cis-diamminedichloroplatinum, *J. Biomed. Sci.* 1 (1994) 131–138.
- [8] G. Spellman, R.W. Staffhorst, K. Versluis, J. Reedijk, B. de Kruijff, Cisplatin complexes with phosphatidylserine in membranes, *Biochemistry* 36 (1997) 10545–10550.
- [9] O. Briz, M.A. Serrano, R.I.R. Macias, J.J.G. Marin, Overcoming cisplatin resistance *in vitro* by a free and liposome-encapsulated bile acid derivative: Bamet-R2, *Int. J. Cancer* 88 (2000) 287–292.
- [10] S. Akiyama, A. Fojo, J.A. Hanover, I. Pastan, M.M. Gottesman, Isolation and genetic characterization of human KB cell lines resistant to multiple drugs, *Somatic Cell Mol. Genet.* 11 (1985) 117–126.
- [11] D.-W. Shen, S. Akiyama, P. Schoenlein, I. Pastan, M.M. Gottesman, Characterization of high-level cisplatin-resistant cell lines established from a human hepatoma cell line and human KB adenocarcinoma cells: cross-resistance and protein changes, *Br. J. Cancer* 71 (1995) 676–683.
- [12] P. Csermely, E. Balint, P.M. Grimley, A. Aszalos, Protein kinase C is involved in the early signal of interferon- $\alpha$  but not of interferon- $\gamma$  in U937 cells, *J. Interferon Res.* 10 (1990) 605–611.
- [13] I.M. Collins, R.B. Scott, Plasma membrane fluidity gradients of human peripheral blood leukocytes, *J. Cell. Physiol.* 144 (1990) 42–51.
- [14] A. Aszalos, G.C. Yang, M.M. Gottesman, Depolymerization of microtubules increases the motional freedom of molecular probes in cellular plasma membranes, *J. Cell Biol.* 100 (1985) 1357–1363.
- [15] J.J. Yin, M.J. Smith, R.M. Epply, A.L. Troy, S.W. Page, J.A. Sphon, Effects of fumonisin B1 and (hydrolyzed) fumonisin backbone API on membranes: a spin-label study, *Arch. Biochem. Biophys.* 335 (1996) 13–22.
- [16] R.A. Schlegel, M. Stevens, K. Lumley-Sapanski, P. Williamson, Altered lipid packing identifies apoptotic thymocytes, *Immunol. Lett.* 36 (1993) 283–288.
- [17] W. Stillwell, S.R. Wassall, A.C. Dumaul, W.D. Ehringer, C.D. Browning, L.G. Jeskin, Use of merocyanine (MC540) in quantifying lipid domains and packing in phospholipid vesicles and tumor cells, *Biochim. Biophys. Acta* 1146 (1993) 136–144.
- [18] D.L. Foxall, J.S. Cohen, J.B. Mitchell, Continuous perfusion of mammalian cells embedded in agarose gel threads, *Exp. Cell Res.* 154 (1984) 521–529.
- [19] D.L. Foxall, J.S. Cohen, NMR studies of perfused cells, *J. Magn. Reson.* 52 (1983) 346–349.
- [20] R. Callaghan, A. Stafford, R.M. Eppard, Increased accumulation of drugs in multidrug resistant cells by alteration of membrane biophysical properties, *Biochim. Biophys. Acta* 1175 (1993) 277–282.
- [21] J. Emsley, S.L. King, J.M. Bergelson, R.C. Liddington, Crystal structure of the I domain from integrin  $\alpha 2\beta 1$ , *J. Biol. Chem.* 272 (1997) 28512–28517.
- [22] M.P. Kozar, M.T. Krahrmer, A. Fox, L. Larsson, J.H. Allton, Lunar dust: a negative control for biomarker analyses of extra-terrestrial samples? *Geochim. Cosmochim. Acta* 65 (2001) 3307–3317.
- [23] O. Kaplan, J.W. Jaroszewski, R. Clarke, C.R. Fairchild, P. Schoenlein, S. Goldenberg, M.M. Gottesman, J.S. Cohen, The multidrug resistance phenotype:  $^{31}\text{P}$  nuclear magnetic resonance characterization and 2-deoxyglucose toxicity, *Cancer Res.* 51 (1991) 1638–1644.
- [24] O. Kaplan, P.C.M. van Zijl, J.S. Cohen, NMR studies of metabolism of cells and perfused organs, *NMR Basic Principles and Progress*, vol. 28, Springer, Berlin, 1992, pp. 3–52.
- [25] S.W. Thomson, L.E. Davis, M. Kornfeld, R.D. Hilgers, J.C. Standerfer, Cisplatin neuropathy, clinical, electrophysiologic, morphology, and toxicologic studies, *Cancer* 54 (1984) 1269–1275.
- [26] K.U. Mahaswari, T. Ramachandran, D. Rajaji, Interaction of cisplatin with planar model membranes—Dose dependent change in electrical characteristics, *Biochim. Biophys. Acta* 1463 (2000) 230–240.
- [27] X.-J. Liang, Y.G. Huang, Physical state changes of membrane lipids in human lung adenocarcinoma A<sub>549</sub> cells and their resistance to cisplatin, *Int. J. Biochem. Cell Biol.* 34 (2002) 1248–1255.
- [28] K.N.J. Burger, W.H.M. Rutger, M. Staffhorst, B.D. Kruijff, Interaction of the anti-cancer drug cisplatin with phosphatidylserine in intact and semi intact cells, *Biochim. Biophys. Acta* 1419 (1999) 43–54.
- [29] H. Timmer-Bosscha, G.A. Hospers, C. Meijer, N.H. Mulder, F.A. Muskiet, I.A. Martini, D.R. Uges, E.G. de Vries, Influence of docosahexaenoic acid on cisplatin resistance in a human small cell lung carcinoma cell line, *J. Natl. Cancer Inst.* 81 (1989) 1069–1075.
- [30] S.S. Chauhan, X.-J. Liang, A.W. Su, A. Pai-Panandiker, D.-W. Shen, J.A. Hanover, M.M. Gottesman, Reduced endocytosis and altered lysosome function in cisplatin resistant cell lines, *Br. J. Cancer* 88 (2003) 1327–1334.
- [31] X.-J. Liang, D.-W. Shen, S. Garfield, M.M. Gottesman, Mislocalization of membrane proteins associated with multidrug resistance in cisplatin-resistant cancer cell lines, *Cancer Res.* 63 (2003) 5909–5916.

### APPENDIX 3

## Steepest changes of a probability-based cost function for delineation of mammographic masses: A validation study

Lisa Kinnard<sup>1,2,3</sup>, Shih-Chung B. Lo<sup>1,2</sup>, Erini Makariou<sup>1</sup>, Teresa Osicka<sup>1,4</sup>,  
Paul Wang<sup>3</sup>, Mohamed F. Chouikha<sup>2</sup>, and Matthew T. Freedman<sup>1</sup>

<sup>1</sup>ISIS Center, Georgetown University Medical Center, Washington, D.C.

<sup>2</sup>Department of Electrical and Computer Engineering, Howard University, Washington, D.C.

<sup>3</sup>Biomedical NMR Laboratory, Department of Radiology, Howard University, Washington, D.C.

<sup>4</sup>Department of Electrical Engineering and Computer Science,  
The Catholic University of America, Washington, D.C.

Submitted to J Medical Physics for consideration as a Technical Report

Please Send the Correspondence to:

Email: lo@isis.imac.georgetown.edu

Dr. Shih-Chung B. Lo  
ISIS Center  
Radiology Department  
Georgetown University  
Box 571479  
Washington, D.C. 20057-1479

### Abstract

The purpose of this work was to develop an automatic boundary detection method for mammographic masses and to rigorously test this method via statistical analysis. The segmentation method utilized a steepest change analysis technique for the determination of the mass boundaries based on a composed probability density cost function. Previous investigators have shown that this function can be utilized to determine the border of mass body. We have further analyzed this method and have discovered that the steepest changes in this function can produce mass delineations to include extended projections. The method was tested on 124 digitized mammograms selected from the University of South Florida's Digital Database for Screening Mammography (DDSM). The segmentation results were validated using overlap, accuracy, sensitivity, and specificity statistics, where the gold standards were manual traces provided by two expert radiologists. We have concluded that the best intensity threshold corresponds to a particular steepest change location within the composed probability density function. We also found that our results are more closely correlated with one expert than with the second expert. These findings were verified *via* Analysis of Variance (ANOVA) testing. The ANOVA tests obtained p-values ranging from  $1.03 \times 10^{-2}$  –  $7.51 \times 10^{-17}$  for the single observer studies,  $2.03 \times 10^{-2}$  –  $9.43 \times 10^{-4}$  for the two observer studies, and results were categorized using three significance levels, i.e.,  $p < 0.001$  (extremely significant),  $p < 0.01$  (very significant), and  $p < 0.05$  (significant), respectively .

**Index Terms:** mass boundary detection, mammography, probability-based cost function

## I. INTRODUCTION

In the United States, breast cancer accounts for one-third of all cancer diagnoses among women and it has the second highest mortality rate of all cancer deaths in women<sup>1</sup>. In several studies it has been shown that only 13% - 29% of suspicious masses were determined to be malignant<sup>2-4</sup>, which indicates that there are high false positive rates for biopsied breast masses. A higher predictive rate is anticipated by combining the mammographer's interpretation and the computer analysis. Other studies have shown that 7.6% - 14% of the patients have mammograms that produce false negative diagnoses<sup>5-6</sup>. Alternatively, a Computer Assisted Diagnosis (CAD<sub>x</sub>) system can serve as a clinical tool for the radiologist and consequently lower the rate of missed breast cancer.

Generally, CAD<sub>x</sub> systems consist of three major stages, namely, segmentation, feature calculation, and classification. Segmentation is arguably one of the most important aspects of CAD<sub>x</sub> - particularly for masses - because a strong diagnostic predictor for masses is shape. Specifically, many malignant masses have ill-defined, and/or spiculated borders and many benign masses have well-defined, rounded borders. Furthermore, breast masses can have unclear borders and are sometimes obscured by glandular tissue in mammograms. During the search for suspicious areas it is possible that masses of this type are overlooked by radiologists. When a specific area is deemed to be suspicious, the radiologist analyzes the overall mass, including its shape and margin characteristics. The margin of a mass is defined as the interface between the mass and surrounding tissue, and is regarded by some as one of the most important factors in determining its significance<sup>7</sup>. Specifically, a spiculated mass consists of a central mass body surrounded by fibrous extensions, hence the resulting stellate shape. In this context, "extension" refers to those portions of the mass containing ill-defined borders, spiculations, fibrous borders, and projections. Although the diameters of these cancers are measured across the central portion of the mass, microscopic analysis of the extensions also reveals associated cancer cells, i.e., the extended projections may contain active mass growth<sup>7,8</sup>. In addition, the features of the extended projections and ill-defined borders are highly useful for identifying masses. Hence, proper segmentation - to include the body and periphery - is extremely important and is essential for the computer to analyze, and in turn, determine the malignancy of the mass in mammographic CAD<sub>x</sub> systems.

Te Brake and Karssemeijer<sup>9</sup> implemented a discrete dynamic contour model, a method similar to snakes, which begins as a set of vertices connected by edges (initial contour) and grows subject to internal and external forces. Li<sup>10</sup> developed a method that employs k-means classification to classify pixels as belonging to the region of interest (ROI) or background. Petrick et al.<sup>11</sup> developed the Density Weighted Contrast Enhancement (DWCE) method, in which series of filters are applied to the image in an attempt to extract masses. Pohlman et al.<sup>12</sup> developed an adaptive region growing method whose similarity criterion is determined from calculations made in 5×5 windows surrounding the pixel of interest. Mendez et al.<sup>13</sup> developed a method, which combined bilateral image subtraction and region growing to segment masses.

Several studies have also used probability-based analysis to segment digitized mammograms. Li et al.<sup>14</sup> developed a segmentation method that first models the histogram of mammograms using a finite generalized Gaussian mixture (FGGM) and then uses a contextual Bayesian relaxation labeling (CBRL) technique to find suspected masses. Furthermore, this method uses the Expectation-Maximization (EM) technique in developing the FGGM model. Comer et al.<sup>15</sup> utilized an EM technique to segment digitized mammograms into homogeneous texture regions by assigning each pixel was to one of a set of classes such that the number incorrectly classified pixels was minimized. Kupinski and Giger<sup>16</sup> developed a method, which combines region growing with probability analysis to determine final segmentation. In their

method, the probability-based function is formed from a specific composed probability density function, determined by a set of image contours produced by the region growing method. This method is a highly effective one and it was implemented by Te Brake and Karssemeijer in their work<sup>9</sup> that compared the results of a model of the discrete dynamic contour model with those of the probability-based method. For this reason we chose to investigate its use as a possible starting point from which a second method could be developed. Consequently for our implementation of this work we discovered an important result, i.e., the steepest changes of a cost function composed from two probability density functions of the regions. It appears that in many cases this result produces contour choices that encapsulate important borders such as mass spiculations and ill-defined borders.

Several CAD<sub>x</sub> classification techniques have been developed. They are described here to underscore the importance of accurate segmentation in CAD<sub>x</sub> studies. Lo et al.<sup>17</sup> has developed an effective analysis method using the circular path neural network technique that was specifically designed to classify the segmented objects and can certainly be extended for the applications related to mass classification. Polakowski et al.<sup>18</sup> used a multilayer perceptron (MLP) neural network to distinguish malignant and benign masses. Both Sahiner et al.<sup>19</sup> and Rangayyan et al.<sup>20</sup> used linear discriminant analysis to distinguish benign masses from malignant masses. While many CAD<sub>x</sub> systems have been developed, the development of fully-automated image segmentation algorithms for breast masses has proven to be a daunting task.

## II. METHODS

A. Segmentation method – Maximum change of cost function as a continuation of probability-based function analysis

As a point of clarification, in this work we refer to the function used to find optimal region growing contours in Kupinski and Giger's study<sup>16</sup> as the probability-based function and we refer our function as the cost function. The two functions are similar; however they differ in terms of the images used in their formation. As an initial segmentation step, region growing is used to aggregate the area of interest<sup>12, 13, 21</sup>, where grayscale intensity is the similarity criterion. This phase of the algorithm starts with seed point whose intensity is high, and nearby pixels with values greater than or equal to this value are included in the region of interest. As the intensity threshold decreases, the region increases in size, therefore there is an inverse relationship between intensity value and contour size. In many cases the region growing method is extremely effective in producing contours that are excellent delineations of mammographic masses. However, the computer is not able to choose the contour that is most highly correlated with the experts' delineations, specifically, those masses that contain ill-defined margins or margins that extend into surrounding fibroglandular tissue. Furthermore, the task of asking a radiologist to visually choose the best contour would be both time intensive and extremely subjective from one radiologist to another.

The segmentation technique described in this work attempts to solve and automate this process by adding a two-dimensional (2D) shadow and probability-based components to the segmentation algorithm. Furthermore, we have devised a steepest descent change analysis method that chooses the best contour that delineates the mass body contour as well as its extended borders, i.e., extensions into spiculations and areas in which the borders are ill-defined or obscured. It has been discovered that the probability-based function is capable of extracting the central portion of the mass density as demonstrated by the previous investigators<sup>16</sup>, and in this work the method has been advanced further such that it can include the extensions of the masses. The enhanced method can produce contours, which closely match expert radiologist traces. Specifically, it has been observed that this technique can select the contour that

accurately represents the mass body contour for a given set of parameters. However, further analysis of the cost function composed from the probability density functions inside and outside of a given contour revealed that the computer could choose a set of three segmentation contour choices from the entire set of contour choices, and later make a final decision from these three choices.

#### 1. Region growing and pre-processing

Initially, a 512×512 pixel area surrounding the mass is cropped. The region growing technique<sup>12, 13, 21</sup> to aggregate the region of interest was employed, where the similarity criterion for our region growing algorithm is grayscale intensity. To start the growth of first region, a seed point was placed at the center of the 512×512 ROI. The region growing process continues by decreasing the intensity value until we have grown a sufficiently large set of contours. Next, the image is multiplied by a 2D trapezoidal membership function with rounded corners whose upper base measures 40 pixels and lower base measures 250 pixels (1 pixel = 50 microns). This function was chosen because it is a good model of the mammographic mass's intensity distribution. Since the ROI's have been cropped such that the mass's center was located at the center of the 512 pixel × 512 pixel area, shadow multiplication emphasizes pixel values at the center of the ROI and suppresses background pixels. The image to which the shadow has been applied is henceforth referred to as the "processed" image. The original image and its processed version were used to compute the highest possibility of its boundaries. The computation method is comprised of two components for a given boundary: (1) formulation of the composed probability as a cost function and (2) evaluation of the cost function.

The contours were grown using the original image as opposed to the processed image and this accounts for a major difference between the current implementation and that implemented by the previous investigators<sup>16</sup>. By using contours generated from the original image a cost function composed from the probability density functions inside and outside of the contours was produced. In many situations, the greatest changes in contour shape and size occur at sudden decreases within the function. In analyzing these steep changes it was observed that the intensity values corresponding to the steep changes typically produced contours that encapsulated both the mass body as well as its spiculated projections or ill-defined margins. This phenomenon would be suppressed if the processed image was used to generate the contour. A more detailed discussion of steep changes within the cost function is forthcoming in section II.A.2.3.

The processed image was mainly used to construct the cost function. A common technique used in mass segmentation studies is to pre-process the images using some type of filtering mechanism<sup>11, 16</sup> in an effort to separate the mass from surrounding fibroglandular tissue. This method could be particularly beneficial to the region growing process because it would aid in preventing the regions from growing into surrounding tissue. Alternatively, the filtering process could impede our goal of attempting to encapsulate a mass's extended borders as well as borders that are ill-defined due to the filtering process's a tendency to create rounded edges on margins that are actually jagged, i.e., spiculated. This phenomenon could potentially defeat the goal of extracting mass borders. For these reasons, we have chosen to aggregate the contours using the original ROI rather its processed version.

#### 2. Formulation of the composed probability as a cost function

In the context of this work, the composed probability is defined as the probability density functions of the pixels inside and outside a contour using a processed and non-processed version of an image. Specifically, for a contour ( $S_i$ ), the composed probability ( $C_i$ ) is calculated:

$$C_i | S_i = \prod_{j=0}^h p(f_i(x,y) | S_i) \times \prod_{j=0}^h p(m_i(x,y) | S_i) \quad (1)$$

The quantity  $f_i(x,y)$  is the set of pixels, which lie inside the contour  $S_i$  (see Fig. 1a), and this area contained processed pixel values. The quantity  $p(f_i(x,y) | S_i)$  is the probability density function of the pixels inside  $S_i$  ( $f_i(x,y)$ ), where 'i' is the intensity threshold used to produce the contours given by the region growing step, and 'h' is the maximum intensity value. The quantity  $m_i(x,y)$  is the set of pixels, which lie outside the contour  $S_i$  (see Fig. 1b), and this area contained non-processed pixels. The quantity  $p(m_i(x,y) | S_i)$  is the probability density function of the pixels outside  $S_i$ , where 'i' is the intensity threshold used to produce the contours given by the region growing step, and 'h' is the maximum intensity value. For implementation purposes, the logarithm of the composed probability of the two regions,  $C_i$  was used.

$$\text{Log}(C_i | S_i) = \log \left( \prod_{j=0}^h p(f_i(x,y) | S_i) \right) + \log \left( \prod_{j=0}^h p(m_i(x,y) | S_i) \right) \quad (2)$$

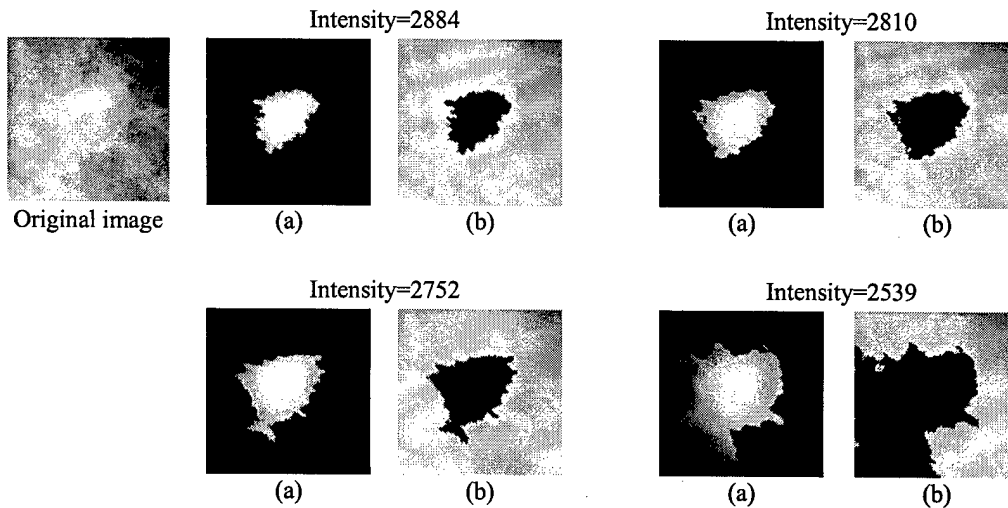


Fig. 1: Four grown contours used to construct the cost function : starts from high intensity thresholds and moves towards low intensity thresholds. Each contour separates the ROI into two parts: (a) Segmented image (based on processed image) used to compute density function  $p(f_i(x,y) | S_i)$  and (b) Masked image (based on non-processed original image) used to compute density function  $p(m_i(x,y) | S_i)$  for four intensity threshold values

### 3. The cost function based on the composed probability density functions

To select the contour that represents the fibrous portion of the mass, it is appropriate to examine the maximum value of the cost function:

$$\arg \max ( \text{Log}(C_i | S_i), S_i, i = 1, \dots, n ) \quad (3)$$

It has been assessed (also by other investigators<sup>9,16</sup>) that the intensity value corresponding to this maximum value is the optimal intensity needed to delineate the mass body contour. However, in the current implementation it was discovered that the intensity threshold corresponding to the maximum value confines the contour to the fibrous portion of the mass, i.e., the mass body. In

the study many of these contours did not include the extended borders. It is therefore, hypothesized that the contour represents the mass's extended borders may well be determined by assessing the greatest changes of the cost function, i.e., locate the steepest value changes within the function:

$$\frac{d}{di} (\text{Log}(C_i | S_i), S_i, i = 1, \dots, n) \quad (4)$$

Based on this assumption, the cost functions associated with masses were analyzed. The analysis reveals that the most likely boundaries of masses associated with expert radiologist traces are usually produced by the intensity value corresponding to the first or second steepest change of value immediately following the maximum value on the cost function (see Fig. 2a). The description of this discovery is given below followed by a validation study described in section II.B and results shown in section III. The overarching goal of the steep descent method is to determine the possibility that a certain contour is the best contour, which represents the mass and its extended borders.

### 3. The definition of steepest change

The term "steepest change" is rather subjective and in the context of this work can be defined as a location between two or more points in the cost function where the values experience a significant change. When the values are plotted as a function of intensity, these significant changes are often visible in the function. In some cases the cost function increases at a slow rate, therefore a potential steepest change location could be missed. The algorithm design compensates for this issue by calculating the difference between values in steps over several values and comparing the results to two threshold values. The difference equation is given by:

$$d(t) = f(z - wt) - f(z - w(t + 1)), \quad t = 0, K, m \quad (5)$$

where  $f$  is the cost function,  $z$  is the maximum intensity,  $w$  is the width of the interval over which the cost function differences are calculated (e.g. - for  $w=5$  differences are calculated every 5 points), and  $m$  is the total number of points in the searchable area divided by  $w$ . Note that " $wt$ " is associated with a specific contour " $i$ " described earlier. If the value of  $d(t)$  yields a value greater than or equal to a given threshold, then the intensity corresponding to this location is determined to be a steepest change location. The threshold algorithm occurs as follows:

**If**  $(d(t) \geq TV_1); t=0, \dots, m$

**Then** choice 1 = intensity where that condition is satisfied.

**If**  $(d(t) \geq TV_2); t=m, \dots, z$

**Then** choice 2 = intensity where that condition is satisfied.

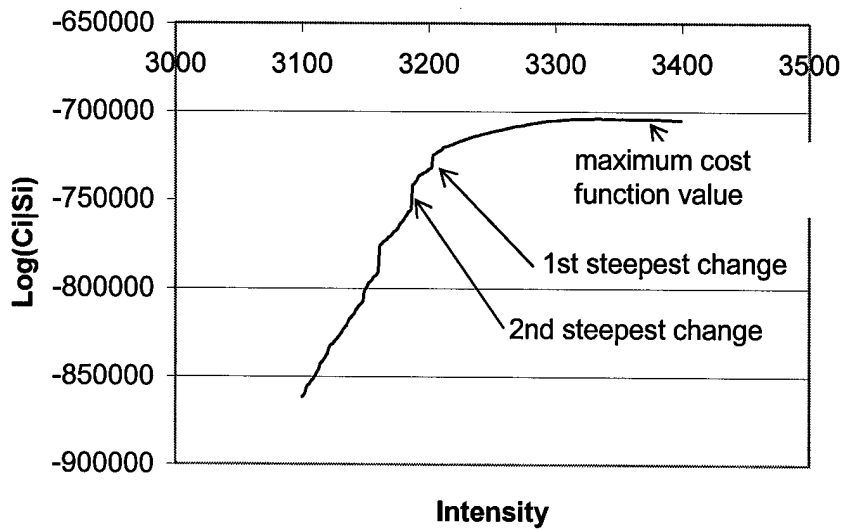
where  $TV_1$  and  $TV_2$  are pre-defined threshold values,  $m$  is the location in the function where the choice 1 condition is satisfied, and  $z$  is the location in the function where the choice 2 condition is satisfied. During the examination of the contour growth with respect to the cost function, the first steepest change (i.e.,  $d(t)_{MC1}$  as choice 1) is determined by  $TV_1$  immediately after the location of the maximum cost function value (corresponding to mass body discussed earlier). The second the steepest change (i.e.,  $d(t)_{MC2}$  as choice 2) is determined by  $TV_2$  after the first steepest change has been established.

As an example Fig. 1a is used to illustrate how the algorithm is carried out. In this figure, the maximum value on the cost function occurs for a grayscale intensity value of approximately 3330. The searching process begins from this maximum point and it is discovered that the first steepest change ( $d(t)_{MC1}$  as choice 1) occurs for a grayscale intensity value approximately equal to 3200. From this point the continue the searching process continues and it is discovered that the second steepest change ( $d(t)_{MC2}$  as choice 2) occurs for a grayscale intensity value

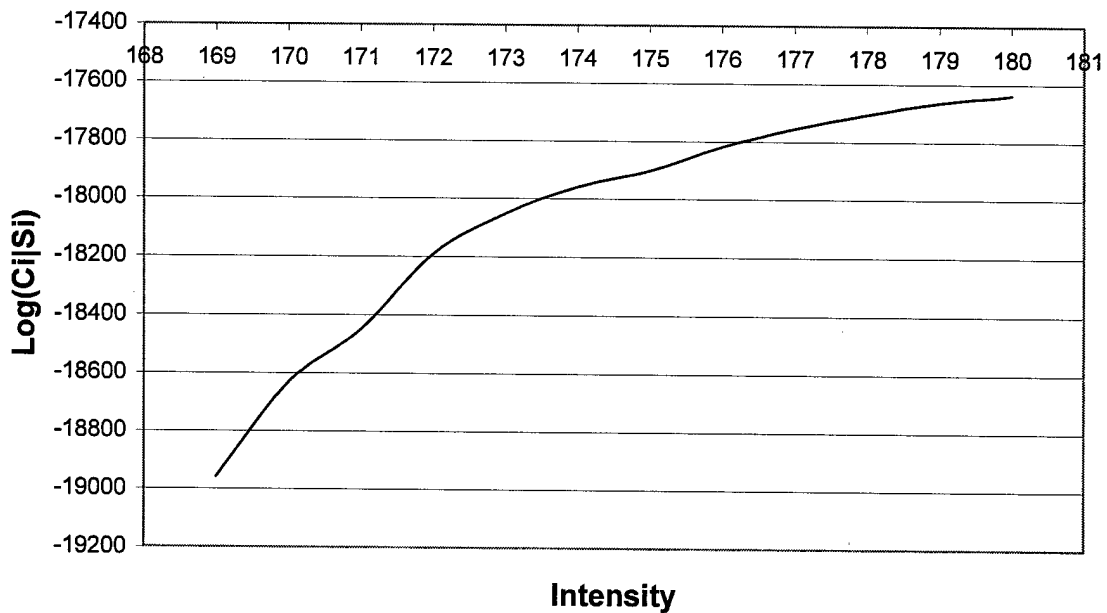
approximately equal to 3175. In summary, intensity values of 3330, 3200, and 3175 can be used to grow 3 potential mass delineation candidates, and the large set of intensity choices has been narrowed to 3 choices. In many cases intensities, which produced the three contour choices gave the following results:

- (1) Intensity corresponding to the maximum value on the cost function: The central body of the mass was encapsulated
  - (2) Intensity corresponding to the first steepest change on the cost function: The central body of the mass + some of its extended borders (i.e., projections and spiculations) was encapsulated
  - (3) Intensity corresponding to the second steepest change on the cost function: The central body of the mass + more extended borders + surrounding fibroglandular tissue encapsulated
- The intensity corresponding to the first steepest change provides the best choice, and an examination of this observation is shown and discussed in sections III and IV of this work.

As stated previously the steep changes within the cost function would be suppressed if the processed image was used to generate the contour, therefore the function would be relatively smooth. This issue is evident in Fig. 2b, which shows a probability-based function produced by contours that were grown using a processed ROI.



(a)



(b)

Fig. 2: (a) Example of cost function with steepest change location indicators (b) Example of a probability-based function without an obvious steepest change location.

### B. Validation method

In several segmentation studies the results were validated using the overlap statistic alone, however, it was necessary to analyze the performance of the steepest change algorithm on the basis of four statistics to verify that the algorithm is indeed capable of categorizing mass and

background pixels correctly. This type of analysis provides helpful information regarding necessary changes for the algorithm's design and can possibly aid in its optimization.

The segmentation method was validated on the basis of overlap, accuracy, sensitivity, and specificity<sup>22, 23</sup>. These statistics are calculated as follows:

$$Overlap = \frac{E \cap P}{E \cup P} \quad (6)$$

$$Accuracy = \frac{N_{TP} + N_{TN}}{N_{TP} + N_{TN} + N_{FP} + N_{FN}} \quad (7)$$

$$Sensitivity = \frac{N_{TP}}{N_{TP} + N_{FN}} \quad (8)$$

$$Specificity = \frac{N_{TN}}{N_{TN} + N_{FP}} \quad (9)$$

where  $E$  is the drawing produced by the expert radiologist,  $P$  is the segmentation result,  $N_{TP}$  is the true positive fraction (part of the image correctly classified as mass),  $N_{TN}$  true negative fraction (part of the image correctly classified as surrounding tissue),  $N_{FP}$  is the false positive fraction (part of the image incorrectly classified as mass), and  $N_{FN}$  is the false negative fraction (part of the image incorrectly classified as surrounding tissue). This method requires a gold standard, or, contour to which the segmentation results can be compared. The gold standards for the experiments performed in this work were mass contours, which have been traced by expert radiologists.

The experiments produced contours for the intensity values resulting from three locations within the cost functions : (1) The intensity for which a value within the cost function is maximum (2) The intensity for which the cost function experiences its first steepest change and (3) The intensity for which the cost function experiences its second steepest change . It has been observed that the intensity for which the cost function experiences its first steepest change produces the contour trace that is most highly correlated with the gold standard traces, regarding overlap and accuracy. In cases for which better results occur at the second steepest change location, there is no significant difference between these results and the results calculated for the first steepest change location. Second, it has been observed that the results are more closely correlated with one expert than with the second expert. These hypotheses were tested using the one-way Analysis of Variance (ANOVA) test<sup>24,25</sup>. In this study, three significance levels (i.e.,  $p < 0.001$ ,  $p < 0.01$ , and  $p < 0.05$ ) were used to categorize the ANOVA results as described in the next section.

### III. EXPERIMENTS AND RESULTS

The following sections describe the database and experiments as well as provide results and ANOVA test results.

#### A. Database

For this study, a total of 124 masses were chosen from the University of South Florida's Digital Database for Screening Mammography (DDSM)<sup>26</sup>. The DDSM films were digitized at 43.5 or 50  $\mu$ m's using either the Howtek or Lumisys digitizers, respectively. The DDSM cases have been ranked by expert radiologists on a scale from 1 to 5, where 1 represents the most subtle masses and 5 represents the most obvious masses. Table 1 lists the distribution of the masses studied according to their subtlety ratings. The images were of varying contrasts and the masses were of varying sizes.

Table 1: Distribution of DDSM masses studied according to their subtlety ratings

Subtlety Category	Cancer	Benign
Number of masses with a rating = 1	5	3
Number of masses with a rating = 2	12	12
Number of masses with a rating = 3	18	17
Number of masses with a rating = 4	9	23
Number of masses with a rating = 5	15	10

The first set of expert traces was provided by an attending physician of the GUMC, and is hereafter referred to as the Expert A traces. The second set of expert traces was provided by the DDSM, and is hereafter referred to as the Expert B traces.

### B. Experiments

As mentioned previously, the term “steepest change” is very subjective and therefore a set of thresholds needed to be set in an effort to define a particular location within the cost function as a “steepest change location”. For this study the following thresholds were experimentally chosen:  $TV_1=1800$ ,  $TV_2=1300$ , where  $TV_1$ = threshold for steepest change location 1 for the cost function, and  $TV_2$  = threshold for steepest change location 2 for the cost function . A number of experiments were performed in an effort to prove that (1) the intensity for which the cost function experiences the first steepest change location produces the contour trace, which is most highly correlated with the gold standard traces with regard to overlap and accuracy. In cases for which the second steepest change location achieves better results, there are no significant differences between the values obtained from the first steepest change location and the second steepest change location. The experiments linked with these hypotheses comprise the studies for a single observer. We have also set out to prove that (2) our results are more closely correlated with one expert than with the second expert. The experiments linked with this hypothesis comprise the studies between two observers. First segmentation results for two malignant cases are presented, followed by segmentation results for two benign cases. Second, the ANOVA results for a set of hypotheses are presented. The contours produced by the maximum value as well as the steepest change locations within the cost functions are labeled as follows:

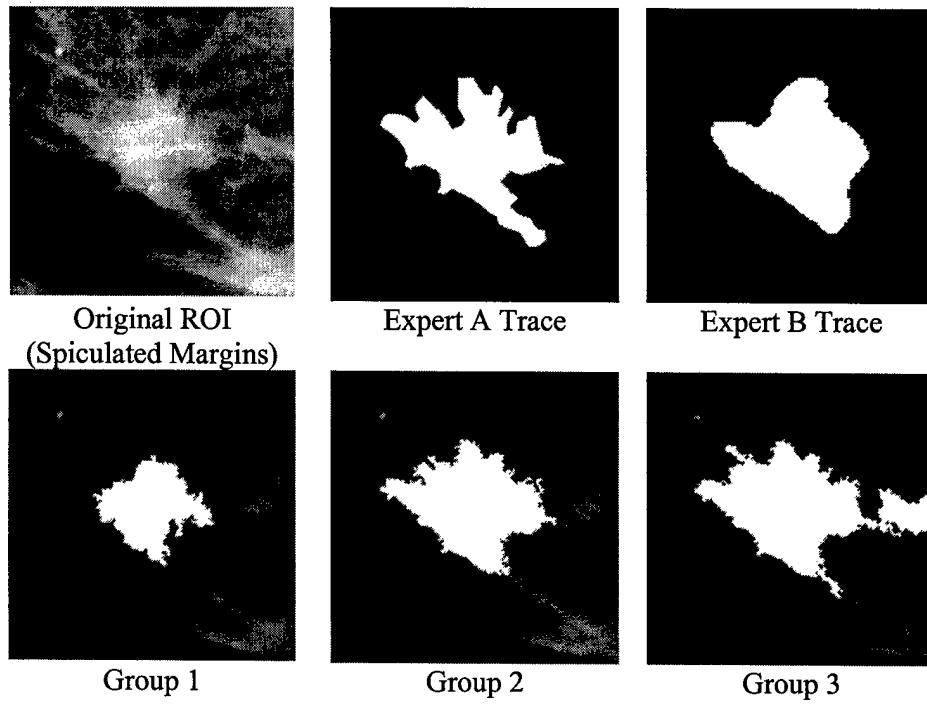
- (1) group 1: The intensity for which a value within the cost function is maximum
- (2) group 2: The intensity for which the cost function experiences its first steepest change
- (3) group 3: The intensity for which the cost function experiences its second steepest change.

### C. Results

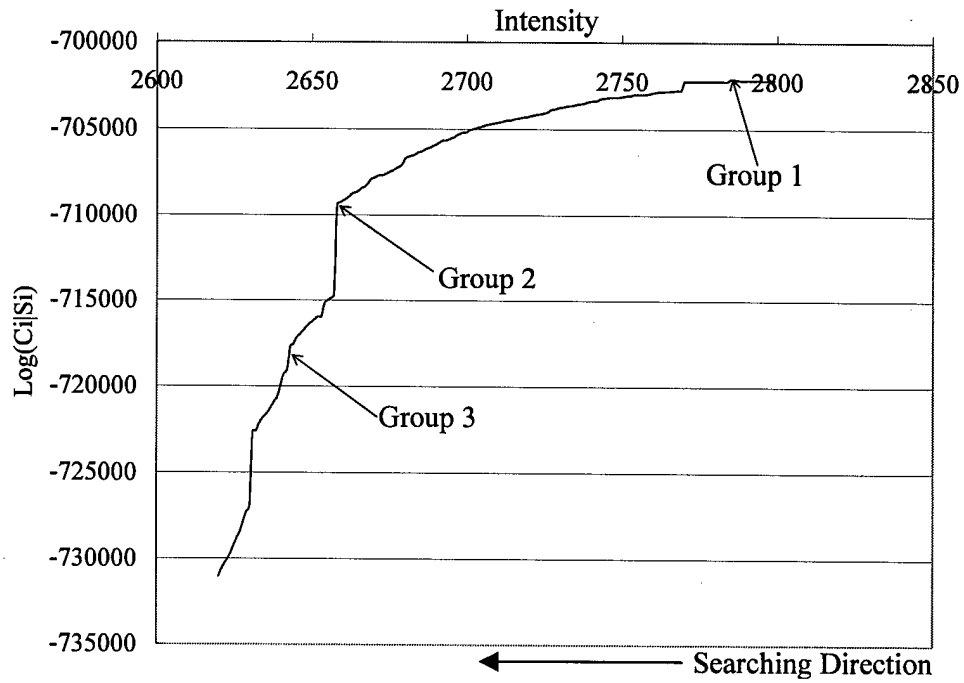
Figures 3-6 display the results for two malignant cases accompanied by their cost functions and results for two benign cases accompanied by their cost functions . The ANOVA results appear in a set of tables (sections 2-4), where each table lists the hypothesis tested along with p-values and their corresponding categorizations. The p-values are categorized in the following way: not significant (NS for  $p > 0.05$ ), significant (S for  $p < 0.05$ ), very significant (VS for  $p < 0.01$ ), and extremely significant (ES for  $p < 0.001$ ). Each p-value table is followed by a second table, which contains the mean values of overlap, accuracy, sensitivity, and specificity for each group. Sections 2 and 3 are identical regarding the experiments, however, the pathologies of the masses are different (section 2 – malignant masses, section 3 – benign masses). Although the experiments are identical they have been separated for clarity purposes.

A larger set of segmentation results has been placed in an image gallery containing 7 malignant mass results (Fig. A1) and 7 benign mass results (Fig. A2). These figures are located in the Appendix.

1. Segmentation results



(a)



(b)

Fig. 3 – (a) Segmentation results for a malignant mass with spiculated margins (subtlety = 2)  
(b) the corresponding cost function

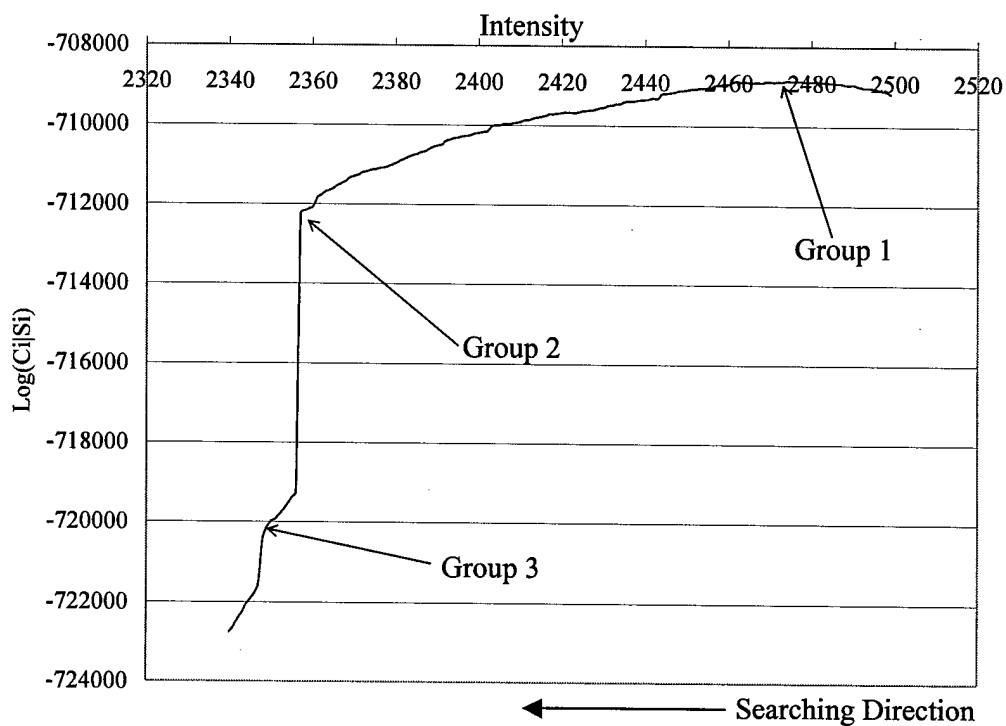
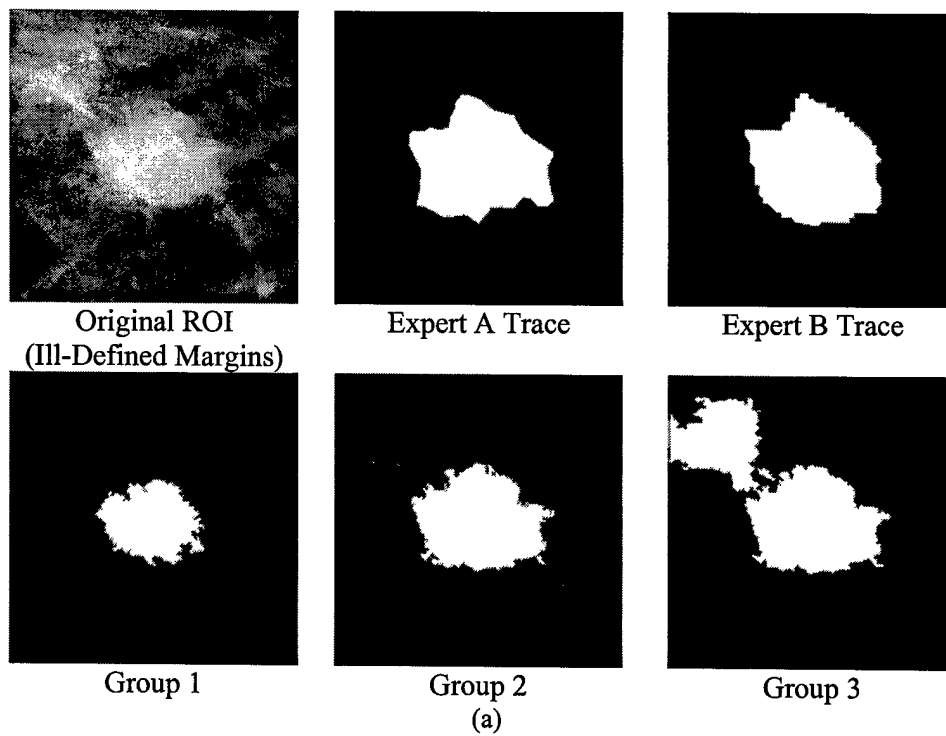


Fig. 4 – (a) Segmentation results for a malignant mass with ill-defined margins (subtlety = 3)  
(b) the corresponding cost function

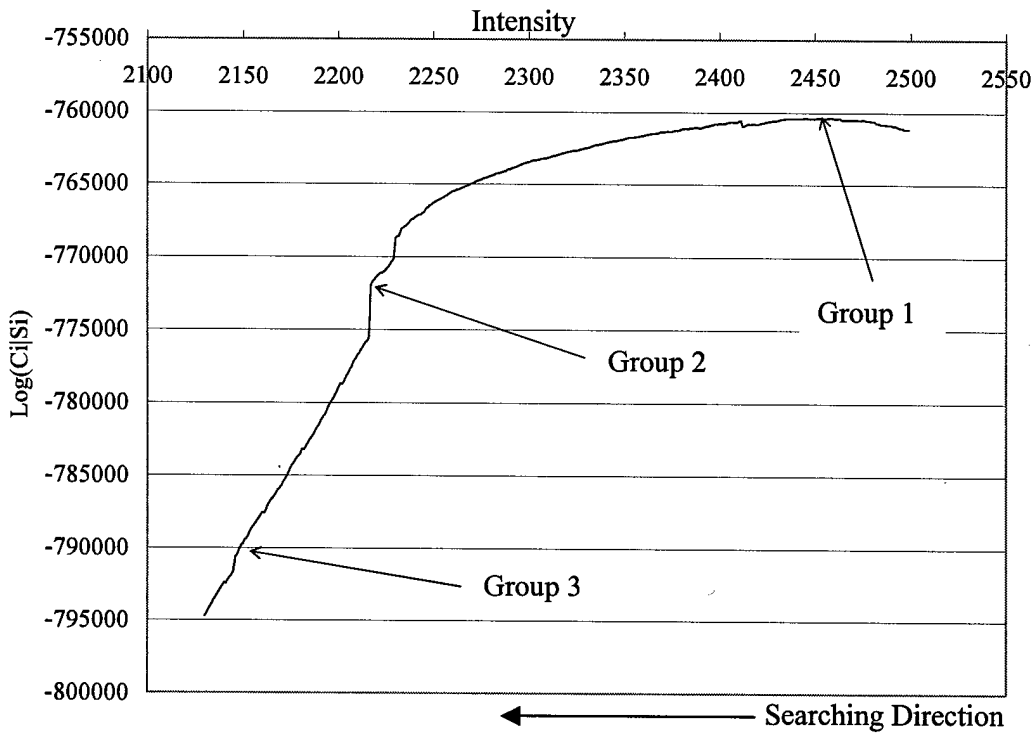
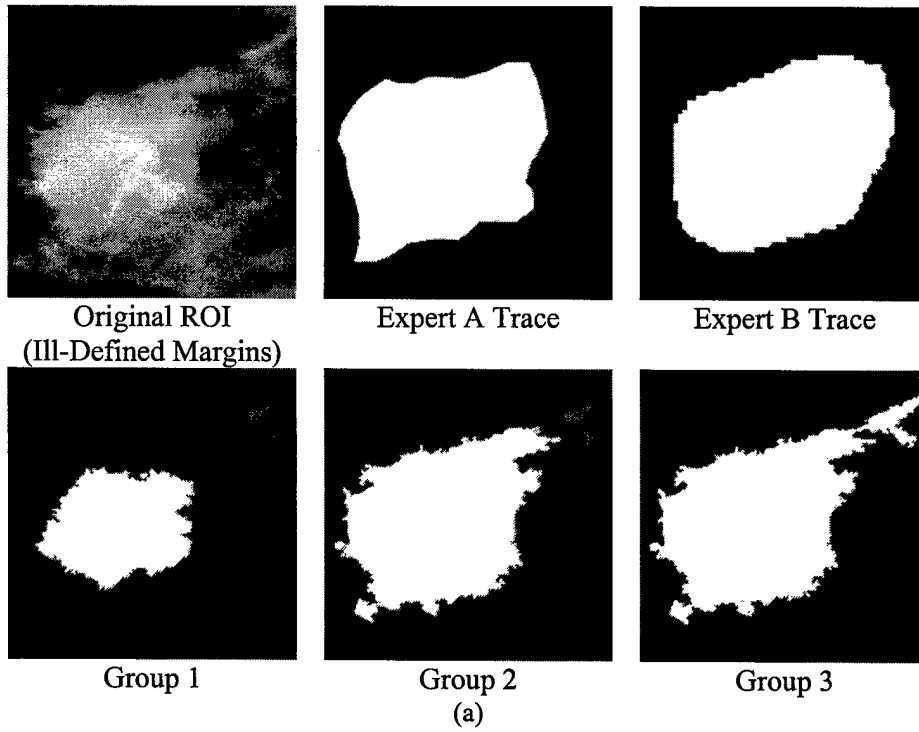


Fig. 5 – (a) Segmentation results for a benign mass with ill-defined margins (subtlety = 3)  
(b) the corresponding cost function

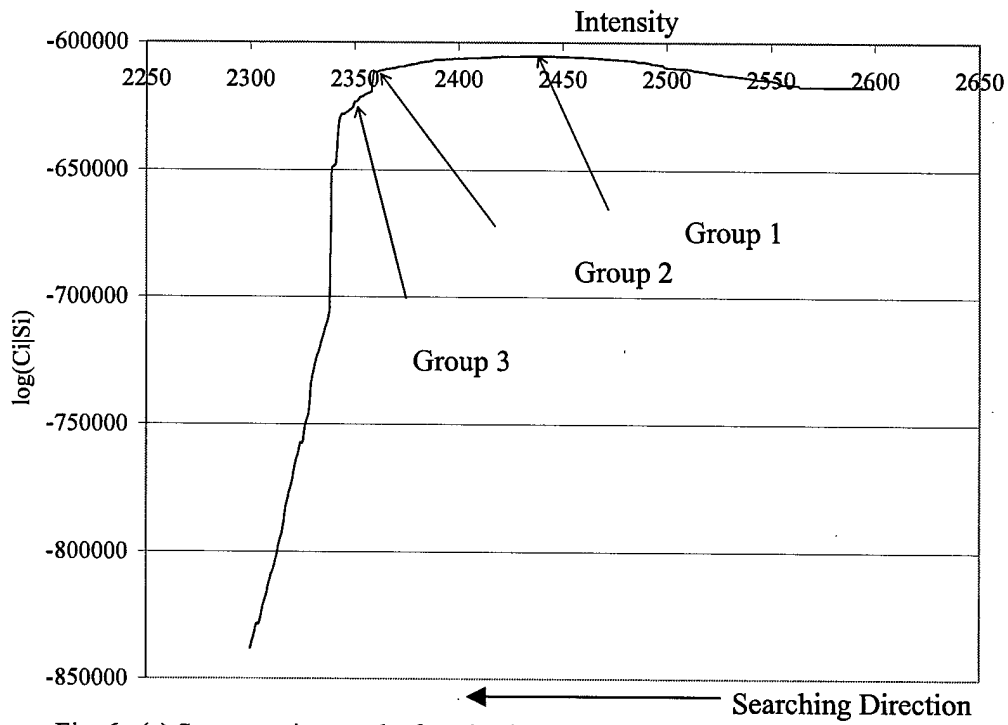
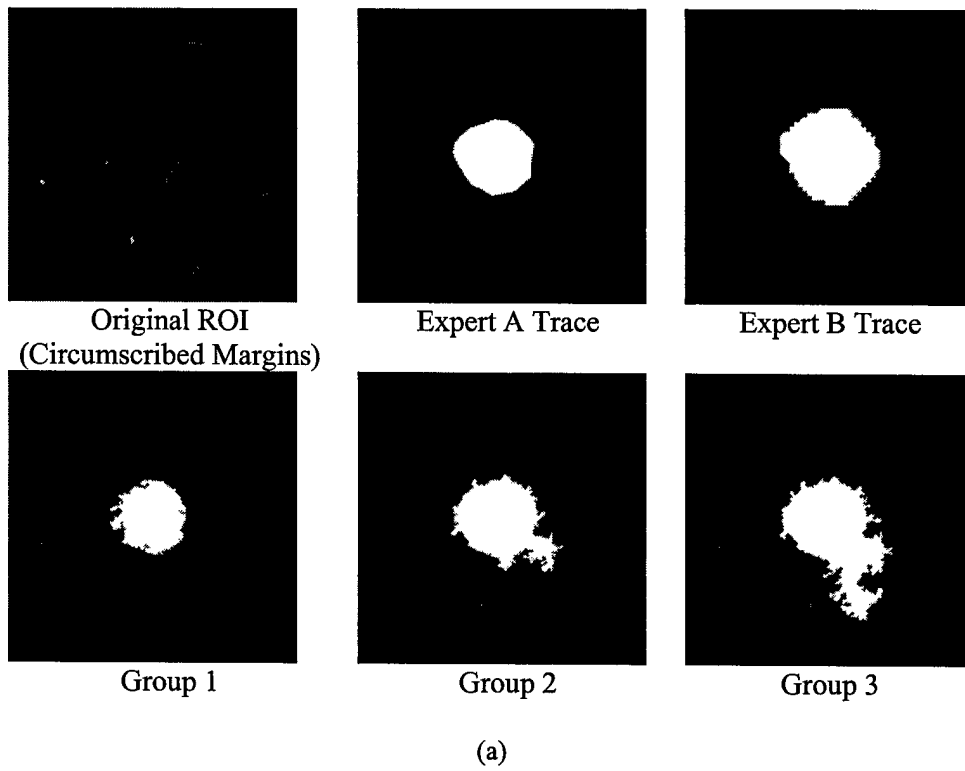


Fig. 6- (a) Segmentation results for a benign mass with circumscribed margins (subtlety = 4)  
(b) the corresponding cost function

2. ANOVA test results for comparison of contour groups with single observer: malignant cases

Table 2: Single observer results (expert A gold standard, malignant masses)

ANOVA Test	P-value (group 1 vs. group 2)	P-value (group 2 vs. group 3)	P-value (group 1 vs. group 3)
Difference between groups (overlap)	$1.78 \times 10^{-4}$ (ES)	$2.91 \times 10^{-2}$ (S)	NS
Difference between groups (accuracy)	NS	$3.14 \times 10^{-2}$ (S)	NS
Difference between groups (sensitivity)	$1.88 \times 10^{-9}$ (ES)	NS	$1.85 \times 10^{-13}$ (ES)
Difference between groups (specificity)	$5.12 \times 10^{-4}$ (ES)	$2.40 \times 10^{-3}$ (VS)	$2.71 \times 10^{-9}$ (ES)

Table 3: Mean values for overlap, accuracy, sensitivity, and specificity (expert A gold standard, malignant masses)

Measurement	Mean Value (group 1)	Mean Value (group 2)	Mean Value (group 3)
Overlap	0.47	0.60	0.53
Accuracy	0.88	0.90	0.87
Sensitivity	0.49	0.75	0.81
Specificity	0.99	0.94	0.88

Table 4: Single observer results (expert B gold standard, malignant masses)

ANOVA Test	P-value (group 1 vs. group 2)	P-value (group 2 vs. group 3)	P-value (group 1 vs. group 3)
Difference between groups (overlap)	$3.96 \times 10^{-6}$ (ES)	NS	$1.58 \times 10^{-4}$
Difference between groups (accuracy)	NS	NS	NS
Difference between groups (sensitivity)	$4.88 \times 10^{-8}$ (ES)	$4.31 \times 10^{-2}$ (S)	$4.25 \times 10^{-12}$ (ES)
Difference between groups (specificity)	$2.70 \times 10^{-4}$ (ES)	$4.36 \times 10^{-4}$ (ES)	$1.44 \times 10^{-7}$ (ES)

Table 5: Mean values for overlap, accuracy, sensitivity, and specificity (expert B gold standard, malignant masses)

Measurement	Mean Value (group 1)	Mean Value (group 2)	Mean Value (group 3)
Overlap	0.38	0.54	0.51
Accuracy	0.83	0.86	0.84
Sensitivity	0.38	0.56	0.60
Specificity	1.00	0.98	0.94

3. ANOVA test results for comparison of contour groups with single observer: benign cases

Table 6: Single observer results (expert A gold standard, benign masses)

ANOVA Test	P-value (group 1 vs. group 2)	P-value (group 2 vs. group 3)	P-value (group 1 vs. group 3)
Difference between groups (overlap)	$3.19 \times 10^{-4}$ (ES)	$8.38 \times 10^{-4}$ (ES)	NS
Difference between groups (accuracy)	NS	$4.73 \times 10^{-3}$ (VS)	$2.51 \times 10^{-3}$ (VS)
Difference between groups (sensitivity)	$1.14 \times 10^{-9}$ (ES)	$1.89 \times 10^{-2}$ (S)	$7.51 \times 10^{-17}$ (ES)
Difference between groups (specificity)	$8.93 \times 10^{-3}$ (VS)	$1.24 \times 10^{-3}$ (VS)	$3.32 \times 10^{-10}$ (ES)

Table 7: Mean values for overlap, accuracy, sensitivity, and specificity (expert A gold standard, benign masses)

Measurement	Mean Value (group 1)	Mean Value (group 2)	Mean Value (group 3)
Overlap	0.46	0.58	0.45
Accuracy	0.90	0.91	0.85
Sensitivity	0.49	0.73	0.82
Specificity	0.99	0.94	0.86

Table 8: Single observer results (expert B gold standard, benign masses)

ANOVA Test	P-value (group 1 vs. group 2)	P-value (group 2 vs. group 3)	P-value (group 1 vs. group 3)
Difference between groups (overlap)	$8.82 \times 10^{-5}$ (ES)	NS	$1.62 \times 10^{-2}$ (S)
Difference between groups (accuracy)	NS	$2.62 \times 10^{-2}$ (S)	$2.48 \times 10^{-2}$ (S)
Difference between groups (sensitivity)	$1.61 \times 10^{-7}$ (ES)	NS	$3.14 \times 10^{-12}$ (ES)
Difference between groups (specificity)	$1.18 \times 10^{-2}$ (S)	$1.27 \times 10^{-2}$ (S)	$1.25 \times 10^{-7}$ (ES)

Table 9: Mean values for overlap, accuracy, sensitivity, and specificity (expert B gold standard, benign masses)

Measurement	Mean Value (group 1)	Mean Value (group 2)	Mean Value (group 3)
Overlap	0.36	0.51	0.44
Accuracy	0.88	0.89	0.83
Sensitivity	0.36	0.61	0.69
Specificity	0.99	0.94	0.86

4. ANOVA test results for comparison of contour groups between two observers

Table 10: Two observer results: expert A vs. expert B, malignant masses

ANOVA Test	P-value (group 1 vs. group 2)	P-value (group 2 vs. group 3)	P-value (group 1 vs. group 3)
Expert A vs. Expert B (overlap)	$3.12 \times 10^{-3}$ (VS)	$3.32 \times 10^{-2}$ (S)	NS
Expert A vs. Expert B (accuracy)	$1.20 \times 10^{-2}$ (S)	$4.46 \times 10^{-2}$ (S)	NS
Expert A vs. Expert B (sensitivity)	$9.43 \times 10^{-4}$ (ES)	$3.38 \times 10^{-4}$ (ES)	$3.67 \times 10^{-4}$ (ES)
Expert A vs. Expert B (specificity)	NS	NS	NS

Table 11: Mean values for overlap, accuracy, sensitivity, and specificity  
(expert A vs. expert B, malignant masses)

Measurement	Mean Value, Expert A (group 1)	Mean Value, Expert B (group 1)	Mean Value, Expert A (group 2)	Mean Value, Expert B (group 2)	Mean Value, Expert A (group 3)	Mean Value, Expert B (group 3)
Overlap	0.49	0.38	0.62	0.55	0.55	0.51
Accuracy	0.89	0.83	0.91	0.87	0.87	0.84
Sensitivity	0.52	0.38	0.75	0.60	0.82	0.68
Specificity	0.99	1.00	0.95	0.97	0.89	0.91

Table 12: Two observer results: expert A vs. expert B, benign masses

ANOVA Test	P-value (group 1 vs. group 2)	P-value (group 2 vs. group 3)	P-value (group 1 vs. group 3)
Expert A vs. Expert B (overlap)	NS	NS	NS
Expert A vs. Expert B (accuracy)	NS	NS	NS
Expert A vs. Expert B (sensitivity)	$3.56 \times 10^{-2}$ (S)	$4.90 \times 10^{-2}$ (S)	$2.03 \times 10^{-2}$ (S)
Expert A vs. Expert B (specificity)	NS	NS	NS

Table 13: Mean values for overlap, accuracy, sensitivity, and specificity:  
expert A vs. expert B, benign masses

Measurement	Mean Value, Expert A (group 1)	Mean Value, Expert B (group 1)	Mean Value, Expert A (group 2)	Mean Value, Expert B (group 2)	Mean Value, Expert A (group 3)	Mean Value, Expert B (group 3)
Overlap	0.42	0.35	0.57	0.50	0.48	0.44
Accuracy	0.90	0.88	0.91	0.89	0.85	0.83
Sensitivity	0.44	0.36	0.71	0.61	0.79	0.69
Specificity	0.99	0.99	0.94	0.94	0.86	0.86

## IV. DISCUSSION

### A. Segmentation Results

From the ROI's shown in Figures 3 and 4 it is evident that the intensity produced by the maximum value is capable of accurately delineating the mass body contour, and in some cases this intensity corresponding to the maximum value produces a contour, which falls inside the mass body contour. This can be potentially problematic because low segmentation sensitivities can produce large errors during the feature calculation and diagnosis phases of CAD<sub>x</sub>. Of the three available segmentation choices for each mass, it appears that the first steepest change location produces the contours with strongest correlation in comparison to both gold standards. These contours appear to cover both the mass body contour as well as the extended borders. In some instances the region grows into some areas that are not declared as mass areas by the gold standards - we call this flooding - and fails to grow into other areas that have been declared as mass areas. Finally, the second steepest change location produces contours that also cover both the mass body contour as well as the extended borders, and, the contours tend to also include surrounding fibroglandular tissue; hence, the flooding phenomenon is a common occurrence. In the cases shown, it is clear that steepest change location 1 produces the best contours, in comparison to the gold standards, however the ANOVA test results allow us to make such a claim. The following discussion is divided into five sections: single observer malignant results, single observer benign results, and two observer results (malignant and benign), algorithm performance, and an additional discussion on methods.

### B. Malignant Cases with Single Observer

For both the Expert A and Expert B gold standards, Tables 2-5 show a statistically significant difference between groups 1 and 2 on the basis of overlap and sensitivity, where the mean values of group 2 were higher than the mean values of group 1 for these statistics. These results are expected because as shown in the figures, the group 2 contours consistently covered more of the mass area (and correctly covered this mass area) as compared to the group 1 contours, according to both experts. There was a statistically significant difference in sensitivity between group 1 and group 3, where the mean of group 3 was higher than the mean of group 1. This is an expected result because out of all the groups, group 3 contours consistently cover the most mass area. For the Expert B gold standard there was a statistically significant difference in overlap between group 1 and group 3, where the mean of group 3 was higher than the mean of group 1. This is an expected result because out of all the groups, group 3 contours correctly cover the most mass area.

### C. Benign Cases with Single Observer

For the Expert A there were statistically significant differences between the group 2 and group 3 traces on the basis of overlap, accuracy, and sensitivity, where the group 2 mean values for overlap and accuracy were higher than those of group 3 (see Tables 6-9). This is an expected result because it is likely that many of the group 3 contours contained flooded areas, which will cause both of these values to be lower than contours without flooded areas. The overlap and sensitivity values for group 2 were significantly higher than those of group 1. This is an expected result because the group 2 contours not only covered more mass area and correctly cover this area. Finally, the group 3 accuracy and sensitivity values were significantly higher than those for group 1. This is an expected result because the group 3 contours not only cover more mass area but also correctly cover this area.

For the Expert B gold standard there were statistically significant differences between the group 2 and group 3 traces on the basis of accuracy and sensitivity, where the group 2 mean values for overlap and accuracy were higher than those of group 3. This is an expected result because it is likely that many of the group 3 contours contained flooded areas, which will cause both of these values to be lower than contours without flooded areas. There were statistically significant differences between group 1 and group 2 on the basis of overlap and sensitivity, where the mean values for group 2 were higher than the mean values for group 1. This is an expected result because the group 2 contours not only cover more mass area and correctly cover this area. There were statistically significant differences between group 3 and group 1 on the basis of overlap and sensitivity, where the mean values for group 3 were higher than those of group 1. This is an expected result because the group 3 contours not only covered more mass area and correctly covered this area.

In nearly all cases for the single observer studies, it was expected that the specificity values for group 1 would always be higher for group 1 than those for groups 2 and 3 because this contour always covered the smallest mass area, consequently its background was always highly correlated with the background areas dictated by the gold standards. Moreover, in some cases the group 2 and group 3 contours grew into areas that were not regarded as mass, but rather were regarded as background, therefore their specificity values had a lower correlation with the gold standard as compared to the group 1 contours.

#### D. Malignant and Benign Cases with Two Observers

For the two observer studies, comparisons were made between experts A and B on a group-by-group basis in an effort to prove that there were significant differences between the two radiologists on the basis of overlap, accuracy, sensitivity, and specificity (see Tables 10-13). For the malignant masses there were statistically significant differences between the two experts on the basis of overlap, accuracy, and sensitivity. There was a statistically significant difference between the two experts for group 3 on the basis of sensitivity. For the benign masses, there were statistically significant differences between the two experts for all three groups on the basis of sensitivity. For all cases Expert A's values were consistently higher than those of Expert B. It is an expected result that there were statistically significant differences between the experts due to their differences in opinion. The fact that Expert A's mean values were higher than those for expert B, however does not warrant the conclusion that Expert A is a more reliable expert; however it does not warrant the conclusion that there is stronger agreement between the computer's results and Expert A's traces. Further, there were less statistically significant differences for the benign cases than for the malignant cases. This is an expected result because in general, benign masses have better defined borders so it was expected that the two experts would strongly agree.

#### E. Algorithm performance

It appears that the thresholds chosen produce first steepest change location intensities that generate contours that are closely correlated with the expert traces. In some instances the second steepest change location is extremely far from the first steepest change location, which implies that the function in question increases very slowly; and, many of the second steepest change location intensities produce contours with flooded areas. For the majority of the cases in which the second steepest change location contour achieves a higher sensitivity value, but not a significantly higher sensitivity value, we can still choose the first steepest change location contour because the difference between the two contours is likely to be negligible.

In analyzing the probability-based cost functions, we found that those functions with very steep changes are typically associated with masses that have well-defined borders while those functions that increase slowly are associated with masses that have ill-defined borders. This phenomenon may make it necessary to develop an adaptive threshold process for the steepest change evaluation such that the functions are grouped into various categories (e.g. – smooth versus steep) because a threshold value that is optimal for the steep function may not be optimal for a smooth function.

#### F. Additional discussion on methods used

In this study it appears that the steepest descent method has the advantage of locating ill-defined margins as well as extensions such as malignant spiculations and projections for mammographic masses. If the human eye is solely used, it can be difficult to separate the mass from surrounding fibroglandular tissue. Therefore, it is believed that this method has the potential to complement the process of reading mammographic films. One of the downfalls of the method is its dependence upon the assumption that masses are generally light in color. This assumption impedes the region growing process because masses that contain darker areas and are surrounded on one or more sides by bright tissue can cause contours to flood into areas that are not actual mass tissue. Typically, this situation occurs for the mass located on the border of the breast region on a mammogram.

All of the segmentation methods surveyed in the introduction of this paper are excellent solutions for the problems the authors set out to solve, however, in some cases it is difficult to make comparisons between different methods without the availability of a set of several visual results. In several studies, the focus was either to detect masses or to distinguish malignant from benign masses. So the validation process did not take the form of a comparison with expert radiologist manual traces, but rather features were calculated on the potential mass candidates and they were later classified as being mass tissue or normal tissue<sup>10,11,12,13</sup>. The purpose of Li's study<sup>14</sup> was to distinguish normal and abnormal tissue so the authors did not provide any statistics such as overlap or accuracy. Nevertheless, the study contains a figure of 60 masses that contain both computer and radiologist annotations to give the reader an idea of the computer algorithm's performance. Te Brake and Karssemeijer's study<sup>9</sup> used the overlap statistic to test the efficacy of their method and they indicated that the central mass area of the mass was delineated by the radiologist and their computer results were compared to these annotations. Kupinski and Giger's study<sup>16</sup> also used the overlap statistic to test the efficacy of their method and set a threshold for which the mass was considered to be successfully segmented. For example, masses whose overlap values are greater than 0.7 imply that there was successful segmentation.

The technical method presented herein shows that the results obtained from the maximization of the composed probability density function (i.e., the cost function) are equivalent to those obtained from previous methods presented by previous investigator. However, the steepest change of the composed probability density function is most close to the radiologist determination.

#### V. CONCLUSION

We have shown that our fully automatic boundary detection method for malignant and benign masses can effectively delineate these masses using intensities, which correspond to the first steepest change location within their cost functions. Additionally, it appears that the method is more highly correlated with one set of expert traces than with a second set of expert traces, regarding the accuracy and overlap statistics. This result shows that inter-observer

variability can be an important factor in segmentation algorithm design, and it has motivated us to seek the opinions of more expert radiologists to test the robustness of our algorithm. The second steepest change location intensity will always yield contours with higher sensitivity values, however, it behooves us to choose the first steepest change location intensity because it avoids the risk of choosing contours that contain substantial flooding. In future work, a worthwhile study would be to run the experiments for different threshold values in an effort to discover the possibility of deriving an optimal threshold procedure. We believe that such a procedure would improve the method of choosing optimal contours.

#### ACKNOWLEDGEMENTS

This work was supported by US Army Grant No.'s DAMD17-03-1-0314, DAMD17-01-1-0267, DAMD 17-00-1-0291, DAAG55-98-1-0187, and NIH grant number RCMI/NCRR/NIH 2G12RR003048. The authors would also like to thank the Referees for their constructive comments and recommendations.

#### REFERENCES

1. J.V. Lacey Jr, S.S. Devesa, L.A. Brinton, "Recent trends in breast cancer incidence and mortality", *Environmental and Molecular Mutagenesis*, **39**, no. 2-3, 82-88 (2002).
2. J.E. Meyer, D.B. Kopans, P.C. Stomper, K.K. Lindfors, "Occult Breast Abnormalities: Percutaneous Preoperative Needle Localization", *Radiology*, **150**, no. 2, 335-337 (1984).
3. A.L. Rosenberg, G.F. Schwartz, S.A. Feig, A.S. Patchefsky, "Clinically occult breast lesions: localization and significance", *Radiology*, **162**, 167-170 (1987).
4. B.C. Yankaskas, M.H. Knelson, M.L. Abernethy, J.T. Cuttino, R.L. Clark, "Needle localization biopsy of occult lesions of the breast", *Investigative Radiology*, **23**, 729-733 (1988).
5. J.A. Harvey, L.L. Fajardo, C.A. Innis, "Previous mammograms in patients with impalpable breast carcinoma: retrospective vs. blinded interpretation", *American Journal of Roentgenology*, **161**, 1167-1172 (1993).
6. J.E. Martin, M. Moskowitz, J.R. Milbrath, "Breast cancer missed by mammography", *American Journal of Roentgenology*, **132**, 737-739, (1979).
7. J.R. Harris, M.E. Lippman, M. Morrow, S. Hellman, "Diseases of the breast", Lippincott-Raven Publishers, Philadelphia, PA, 80-81 (1996).
8. J.E. Martin, "Atlas of mammography: histologic and mammographic correlations (second edition)", Williams and Wilkins, Baltimore, MD, p. 87 (1988).
9. G.M. te Brake, N. Karssemeijer, "Segmentation of suspicious densities in digital mammograms", *Medical Physics*, **28**, 259-266 (2001).
10. L. Li, Y. Zheng, L. Zhang, R. Clark, "False-positive reduction in CAD mass detection using a competitive classification strategy", *Medical Physics*, **28**, 250-258 (2001).
11. N. Petrick, H.-P. Chan, B. Sahiner, D. Wei, "An adaptive density-weighted contrast enhancement filter for mammographic breast mass detection", *IEEE Trans. on Med. Imag.*, **15**, 59-67 (1996).
12. S. Pohlman, K.A. Powell, N.A. Obuchowski, W.A. Chilcote, S. Grundfest-Broniatowski, "Quantitative classification of breast tumors in digitized mammograms", *Medical Physics*, **23**, no. 8, 1336-1345, (1996).
13. A.J. Méndez, P.G. Tahoces, M.J. Lado, M. Souto, J.J. Vidal, "Computer-aided diagnosis: Automatic detection of malignant masses in digitized mammograms", *Medical Physics*, **25**, 957-964 (1998).

14. H. Li, Y. Wang, K.J. R. Liu, S.-C. B. Lo, M.T. Freedman, "Computerized radiographic mass detection - part I: lesion site selection by morphological enhancement and contextual segmentation", *IEEE Trans. on Med. Imag.*, **20**, 289-301 (2001).
15. M.L. Comer, S. Liu, E.J. Delp, "Statistical segmentation of mammograms", digital mammography '96: proceedings of the 3rd international workshop on digital mammography, Chicago, IL, 475-478 (9-12 June 1996).
16. M.A. Kupinski, M.L. Giger, "Automated seeded lesion segmentation on digital mammograms", *IEEE Trans. on Med. Imag.*, **17**, no. 4, 510-517 (1998).
17. S.-C. B. Lo, H. Li, Y. Wang., L. Kinnard, and M.T. Freedman, "A multiple circular path convolution neural network system for detection of mammographic masses", *IEEE Transactions on Medical Imaging*, **21**, 150-158 (2002).
18. W.E. Polakowski, D.A. Cournoyer, S.K. Rogers , M.P. DeSimio, D.W. Ruck, J.W. Hoffmeister, R.A. Raines, "Computer-Aided Breast Cancer Detection and Diagnosis of Masses Using Difference of Gaussians and Derivative-Based Feature Saliency", *IEEE Transactions on Medical Imaging*, **16**, pp. 811-819 (1997).
19. B. Sahiner, H.-P. Chan, N. Petrick, M.A. Helvie, L.M. Hadjiiski, "Improvement of mammographic mass characterization using spiculation measures and morphological features", *Medical Physics*, **28**, pp. 1455-1465 (2001).
20. R.M. Rangayyan, N.M. El-Faramawy, J.E. Leo Desautels, O.A. Alim, "Measures of Acutance and Shape for Classification of Breast Tumors", *IEEE Transactions on Medical Imaging*, **16**, pp. 799-810 (1997).
21. B. Sahiner, H.-P. Chan, D. Wei, N. Petrick, M.A. Helvie, D.D. Adler, M.M. Goodsit, "Image feature selection by a genetic algorithm: Application to classification of mass and normal breast tissue", *Medical Physics*, **23**, pp. 1671-1684 (1996).
22. J. Suckling, D.R. Dance, E. Moskovic, D.J. Lewis, S.G. Blacker, "Segmentation of mammograms using multiple linked self-organizing neural networks", *Medical Physics*, **22**, 145-152, (1995).
23. B. Van Ginneken, "Automatic segmentation of lung fields in chest radiographs", *Medical Physics*, **27**, 2445-2455, (2000).
24. D. Downing , J. Clark, "Statistics the Easy Way, 2<sup>nd</sup> ed.", Hauppauge, NY: Barron's Educational Series, 184-206 (1989).
25. W. Hopkins, (2002) *A New View of Statistics: P values and statistical significance*. [Online]. Available: [www.sportsci.org/resource/stats/pvalues.html](http://www.sportsci.org/resource/stats/pvalues.html).
26. M. Heath, K.W. Bowyer, D. Kopans et al., "Current status of the digital database for screening mammography", *Digital Mammography*, Kluwer Academic Publishers, 457-460 (1998).

**APPENDIX A – Gallery of Segmentation Results**

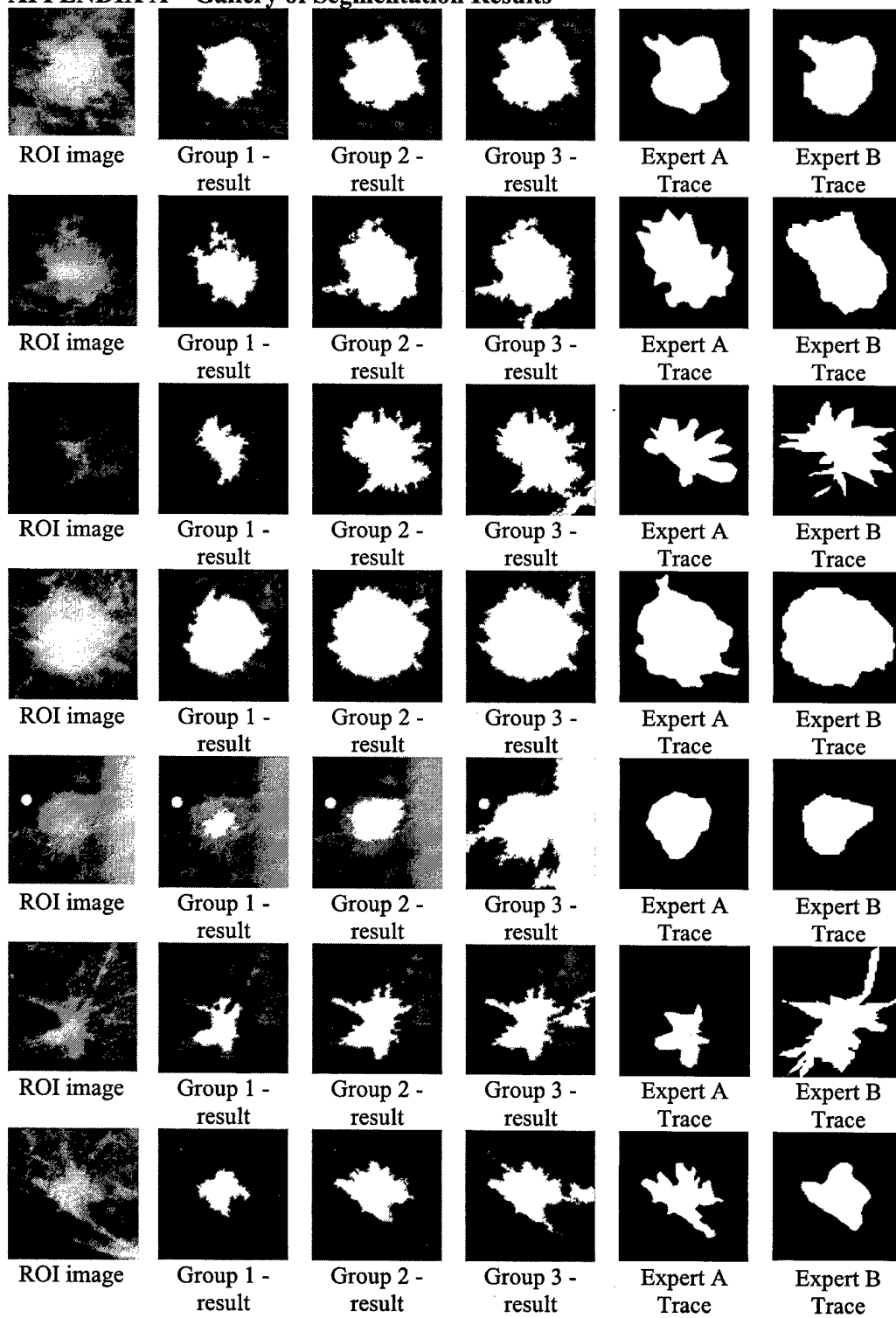


Fig. A1 – Segmentation results for a set of malignant masses

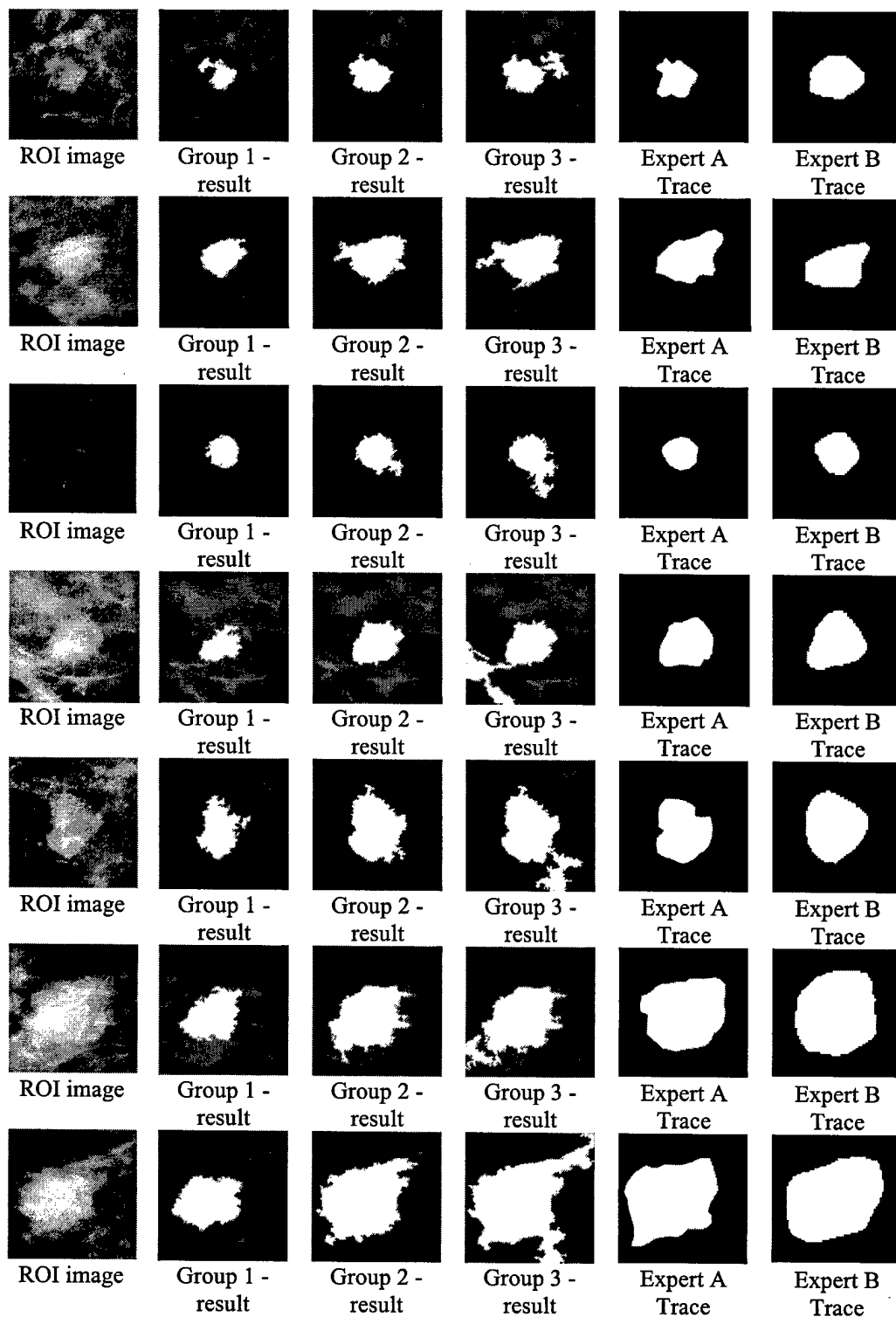


Fig. A2 – Segmentation results for a set of benign masses

Workshop on Dynamic Spectroscopy and Measurement of Physiology and Function  
International Society of Magnetic Resonance in Medicine, September 6-8, 2003, Orlando, FL

A Pharmacokinetic Study of Trifluoperazine Crossing Blood-Brain-Barrier Due to P-glycoprotein Modulation

<sup>1</sup>Paul C Wang, <sup>2</sup>Adorjan Aszalos, <sup>1</sup>Ercheng Li, <sup>1</sup>Renshu Zhang, <sup>1</sup>Huafu Song

<sup>1</sup>Department of Radiology, Howard University, Washington, DC

<sup>2</sup>National Cancer Institute, Bethesda, MD, and Food and Drug Administration, College Park, MD

**INTRODUCTION** Elderly patients and patients with cancer are often treated with combination therapy such as depression, and cardiopulmonary diseases in addition to for their primary symptoms. The potential for drug-drug interaction under these conditions is high. Such interactions may cause changes in the pharmacokinetics, especially for drugs with narrow therapeutic indices (1, 2). These changes can alter efficacy and toxicity of the administered drugs. Drug-drug interactions may occur due to common metabolic pathways, but also due to interference at the P-glycoprotein (Pgp) level. Pgp, which is a nonspecific transport protein, is expressed constitutively at the blood-brain-barrier (BBB), intestine, kidney, and liver (3). Interaction at the blood-brain barrier may occur if Pgp is blocked by a drug and a concomitantly administered second drug, which would not penetrate brain if administered singly, can then penetrate the brain freely (4,5). The potential for drug-drug interactions is not routinely studied at the Pgp level during drug development. Its presence is assumed only after unexpected clinical symptoms. In this study, we have used a dynamic NMR method based on detection of a fluorinated drug, trifluoperazine (TFP), in the brain, in combinations with an immune suppressor, cyclosporin A to demonstrate the drug penetration through the blood-brain-barrier due to Pgp modulation.

**METHODS** Sprague-Dawley rats, weight 200 g, were used. The rats were anesthetized by i.p. injection of sodium pentobarbital 40 mg/kg. After anesthesia, a Pgp modulator cyclosporin A (15 mg/kg) was administered through the tail vein. Fifteen minute later, trifluoperazine (25 mg/kg) was injected. For detection of trifluoperazine in the brain, <sup>19</sup>F NMR studies were performed using 4.7 T, 33 cm horizontal bore NMR machine. A 22 mm x 17 mm surface coil was positioned immediately adjacent to the rat skull. A small bulb containing trifluoroacetic acid was used as an external reference. After shimming and tuning, a series of 10 minutes spectra were obtained. The repetition time was one second.

**RESULTS** In Figure 1, the spectrum A shows a control, in which only TFP was administered. The spectrum B shows an increase amount of TFP crossing BBB after co-administering a Pgp modulator, cyclosporin A. This demonstrates the synergistic effect of cyclosporin A with TFP. Figure 2 shows nine continuous <sup>19</sup>F spectra from the rat brain after administering cyclosporin A and TFP. Each spectrum takes 10 minutes. The first spectrum in the Figure 2 is taken before TFP injection as a baseline. For the second 10 minutes during the TFP injection, there is an increase of fluorine signal. The following spectra 3-9 show the accumulation of TFP and gradual decreasing of fluorine signal due to metabolism.

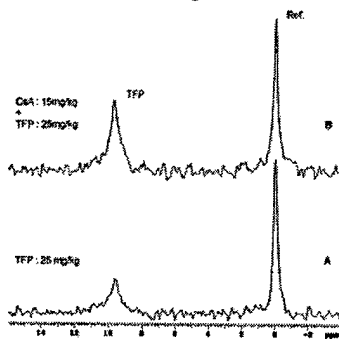


Figure 1

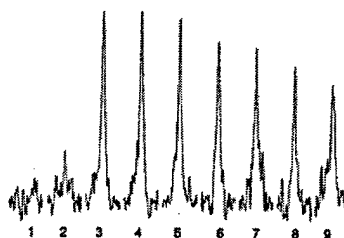


Figure 2

**DISCUSSION** This experiment has demonstrated that concomitantly administered a Pgp modulator enhanced TFP, an antipsychotic drug, crossing BBB in vivo. It also demonstrated the pharmacokinetics of TFP accumulation in the brain. The pharmacology of this noninvasive model for realizing opening of the BBB in case of possible drug-drug interaction at the Pgp level was based on drug know to modulate Pgp and on the drug which can be detected by <sup>19</sup>F NMR spectroscopy. In case of polypharmacy, like with elderly or cancer patients, drug-drug interaction is not always understood. The noninvasive dynamic NMR spectroscopy study of drug-drug interactions can be a very useful tool in drug development.

**REFERENCES**

1. Balis FM, Clin. Pharmacokin., 11, 223-235, 1986
2. Ibrahim S, Peggins J, Knapton A, Licht T, Aszalos A, Anticancer Res., 21, 847-856, 2001
3. Gottesman MM, Fojo T and Bates SE, Nature Reviews, 2, 48-58, 2002
4. Schinkel A, Wagenar F, Mol C and Van Deemter L, J. Clin. Invest., 97,2517-2524, 1996
5. Tatsura T, Naito M, Ohhara T, Sugawara I and Tsuruo T, J. Biol. Chem., 267,20383-20391, 1992

(This work was supported by US Army grant DAMA17-00-1-0291)

Twelfth Annual Meeting of the International Society of Magnetic Resonance in Medicine, May 17-21, Kyoto, Japan

### A NMR Study of Trifluoperazine Crossing Blood-Brain-Barrier Due to P-glycoprotein Modulation

<sup>1</sup>Paul C Wang, <sup>2</sup>Adorjan Aszalos, <sup>1</sup>Ercheng Li, <sup>1</sup>Renshu Zhang, <sup>1</sup>Huafu Song, <sup>1</sup>Raymond Malveaux

<sup>1</sup>Department of Radiology, Howard University, Washington, DC

<sup>2</sup>National Cancer Institute, Bethesda, MD

#### INTRODUCTION

Elderly patients and patients with cancer are often treated with a combination of therapies for secondary illnesses such as depression, and cardiopulmonary diseases in addition to their primary illnesses. The potential for drug-drug interaction under these conditions is high. Such interactions may cause changes in the pharmacokinetics, especially for drugs with narrow therapeutic indices (1, 2). These changes can alter efficacy and toxicity of the administered drugs. Drug-drug interactions may occur due to interaction of common metabolic pathways, but can also be caused by interference at the P-glycoprotein (Pgp) level. Pgp, which is a nonspecific transport protein, is expressed constitutively at the blood-brain-barrier (BBB), intestine, kidney, and liver (3). Interaction at the blood-brain barrier may occur if Pgp is blocked by a drug, allowing a concomitantly administered second drug, which would not penetrate brain if administered singly, to be able to penetrate the brain freely (4,5). The potential for drug-drug interactions is not routinely studied at the Pgp level during drug development. Its presence is assumed only after unexpected clinical symptoms arise. In this study, we used a dynamic NMR method based on detection of a fluorinated drug, trifluoperazine (TFP), in combination with an immune suppressor, cyclosporin A (CsA), to monitor the drug penetration through the blood-brain-barrier due to Pgp modulation (6).

#### METHODS

Sprague-Dawley rats, weight 100-400 g, were used. The rats were first anesthetized by i.p. injection of sodium pentobarbital (40 mg/kg). A catheter (0.26 mm i.d.) was then inserted into the tail vein for later drug infusions. A Pgp modulator, cyclosporin A (15 mg/kg) was administered 15 min before trifluoperazine (25 mg/kg) was injected. <sup>19</sup>F NMR using a Varian 4.7 T machine was utilized to detect trifluoperazine in the brain. A 22 x 17 mm RF coil was positioned immediately adjacent to the rat skull. A small bulb containing trifluoroacetic acid was used as an external reference. After shimming and tuning, a series of 10 minutes spectra were obtained. The repetition time was one second. The same animal was used as control without cyclosporin A. The test results of five different rats were averaged for each data point.

#### RESULTS

Figure 1 shows TFP crossing BBB as function of TFP dosages ranging from 5 to 35 mg/kg. This demonstrates that <sup>19</sup>F signal can be used as a reliable probe to monitor TFP accumulation in the brain. In Figure 2, the spectrum A shows a control, in which only TFP was administered. The spectrum B shows a 22% increase of TFP crossing BBB in a 200 gm rat after co-administering a Pgp modulator, cyclosporin A. Figure 3 shows the increased amount of TFP crossing BBB as function of age (or body weight). Younger rats weighing below 100 gm showed no increase of TFP penetration. However, for older adult rats weighing more than 200 gm, a 20-25% increase of TFP crossing BBB was evident.

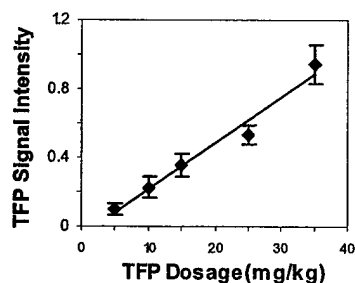


Figure 1

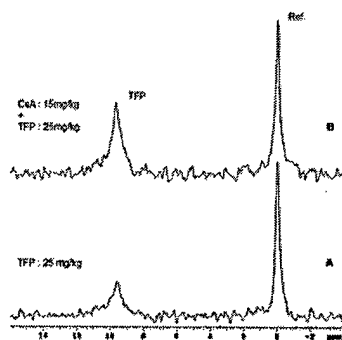


Figure 2

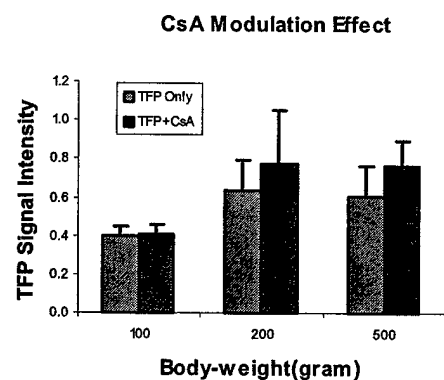


Figure 3

#### DISCUSSION

This experiment has demonstrated that a concomitantly administered Pgp modulator enhanced the amount of TFP, an antipsychotic drug, to cross blood-brain-barrier in vivo. The pharmacology of this noninvasive model for increasing the crossing of drugs over the BBB due to drug-drug interactions was based on previously attained knowledge about how to modulate Pgp, and also because the drug was able to be detected by in vivo <sup>19</sup>F NMR spectroscopy. It also demonstrated that Pgp modulation is more problematic for older rats. In the case of polypharmacy, particularly for elderly or cancer patients, drug-drug interaction is not always understood. The noninvasive dynamic NMR technique can be a very useful tool to study multidrug interactions in drug development.

#### REFERENCES

- Balis FM, Clin. Pharmacokin., 11, 223-235, 1986
- Ibrahim S, Peggins J, Knapton A, Licht T, Aszalos A, Anticancer Res., 21, 847-856, 2001
- Gottesman MM, Fojo T and Bates SE, Nature Reviews, 2, 48-58, 2002
- Schinkel A, Wagenar F, Mol C and Van Deemter L, J. Clin. Invest., 97,2517-2524, 1996
- Tatsura T, Naito M, Ohhara T, Sugawara I and Tsuruo T, J. Biol. Chem., 267,20383-20391, 1992
- Lindquist DM, Dachtler M, Hawk RM, Karson CN, Albert K, Komoroski RA, Magn Reson Med, 43, 756-759, 2000 (This work was supported by grants: DAMD-17-00-1-0291 and RCMI/NCRR/NIH 2G12RR003048).

The Third Annual Meeting of the Society for Molecular Imaging, September 9-12, St. Louis, MO

Control/Tracking Number : 04-A-452-SMI  
Activity :Abstract  
Current Date/Time : 6/28/2004 10:23:49 AM

**MR Image Enhancement by Tumor Cell Targeted Immunoliposome Complex Delivered Contrast Agent**

Paul C. Wang, PhD<sup>1</sup>, Ercheng Li, PhD<sup>1</sup>, Renshu Zhang, MD<sup>1</sup>, Huaifu Song, BS<sup>1</sup>, Kathleen Pirollo, PhD<sup>2</sup>, Esther H. Chang, PhD<sup>2</sup>.  
<sup>1</sup>Howard University, USA, <sup>2</sup>Georgetown University, USA.

Paramagnetic contrast agents such as gadolinium chelates have been used to enhance MR image contrast by disturbing the local magnetic field and the magnetization of surrounding proton spins. The uptake of the contrast agent into the tumor interstitial space is based upon permeation of contrast agent through arterioles and its diffusion within intercellular space. The uptake process is not specific. We have made use of a cationic immunoliposome system that employs a single-chain antibody variable fragment (scFv) to target a liposome-contrast agent complex preferentially to the human transferrin receptor (TfR) of cancer cell. Cationic liposomes are composed of positively charged lipid bilayers that are complexed to gadolinium chelates, Magnevist, by simple mixing. The resulting complex has a net positive charge that facilitates transfection of the cells, and a small size that allows penetration through the capillaries to the tumor cells. Magnevist is diluted in water and added to scFv-Lip at a defined ratio. The equivalent dose of Magnevist is 0.3 mM/kg. Human leukemic cells K562 were transfected with the solution containing TfR-scFv-Lip-Magnevist complex, or Magnevist only. After transfection, the cells were cultured for additional 48 hours. The cells then were pelleted for MRI study. T1-weighted MR images (SE TR/TE, 1000ms/13ms) of cell pellets show an intensity increase of 6 folds for TfR-scFv-Lip-Magnevist complex compared to Magnevist only. Also, a study of transfection time shows the intensity change reaches a plateau after 60 minutes exposure. The advantages of targeted liposome as contrast agent delivery vehicle are its low toxicity, simplicity of preparation, its relative stability, and most significantly its ability to preferentially target tumor cells and efficiently transfer the contrast agent to them. Therefore use of this deliver system has the potential to enhance the sensitivity of the contrast agent.

**Author Disclosure Block:** P.C. Wang, None.

**Topic (Complete):** Enhancing Delivery and Traversing Barriers

**Keywords (Complete):** magnetic resonance imaging ; contrast enhancement ; liposome ; single-chain antibody fragment variable ; transferrin receptor

34<sup>th</sup> Annual Meeting of the Society of Neuroscience. October 23-27, 2004, San Diego, CA

**In-Vivo and In-vitro Stereological Analysis of Hippocampal and Brain Volumes in Young and Old APP/PS1 Mice Using Magnetic Resonance Neuroimages**

Manaye, K.F.<sup>1\*</sup>, Wang, P.<sup>1</sup>, O'Neil J<sup>1</sup>, Armand Oei<sup>1</sup>, Huaifu Song<sup>1</sup>, Tizabi Y<sup>1</sup>, Ingram, D.K.<sup>2</sup>, Mouton, P.R.<sup>2,3</sup>

1Howard University School of Medicine;

2Laboratory of Experimental Gerontology, National Institute on Aging, NIH, Baltimore, MD;

3Stereology Resource Center, Chester, MD.

Previous stereological studies of cortical volumes in human brains at autopsy show only slight changes during normal aging. In contrast, autopsied brains from patients suffering neurological disease, including acquired immunodeficiency syndrome (AIDS) and Alzheimer's disease (AD), show significant loss (atrophy) of cortical and whole brain volumes compared to age-matched controls. In the case of AD the severity of cortical atrophy is highly correlated to the severity of cognitive impairment (Mouton et al., *Neurobiol Aging* 19:371-377, 1998). Early detection of cortical atrophy would help to better understand the natural history of neurodegenerative changes and improve the efficacy of strategies for therapeutic management of these diseases. We addressed this issue using high-resolution magnetic resonance imaging (MRI) to visualize the right hippocampal formation and right hemisphere of mice double transgenic for two mutant proteins associated with AD (amyloid precursor protein and presenilin-1). Young and aged dtg APP/PS1 mice were imaged using a spin-echo T1-weighted MRI imaging technique.

Total volumes of right hemisphere (V<sub>brain</sub>), and total right hippocampal formation (V<sub>HF</sub>) were estimated from systematic-random series of coronal MRI images using point counting-Cavalieri method. We estimated the hemispheric and hippocampal formation volumes in the brains perfused and processed for histology, and the estimates of V<sub>brain</sub>, and V<sub>HF</sub> were repeated after final tissue processing. The preliminary findings In-vivo for WT and dtg APP/PS1 mice show a 15 % reduction in volume of hippocampal formation and no change in the volume of the brain. The In-vitro analysis showed consistent shrinkage of 65-75% for each examined brains.

These stereological studies of mouse MRI images document the changes in brain volumes associated with agonal and tissue processing, and support quantitative neuroimaging for characterization of rodent models of neurological disease. Additional studies will address whether the age-related changes in cortical brain volumes in dtg APP/PS1 mice mimic the patterns that occur in AD.

Supported by intramural and extramural funding from the U.S. Public Health Service. DAMD-17-00-1-0291 and RCMI/NCRR/NIH 2G12RR003048